Nuclear Science and Techniques (2024) 35:213
https://doi.org/10.1007/s41365-024-01587-y

Bρ-defined isochronous mass spectrometry at the storage ring CSRe

Xu Zhou[1,2] · Meng Wang[1,2] · Yu-Hu Zhang[1,2] · Xiao-Hong Zhou[1,2] · Xin-Liang Yan[1,2] · Yuan-Ming Xing[1,2]

Received: 4 July 2024 / Revised: 18 August 2024 / Accepted: 16 September 2024 / Published online: 25 November 2024

Abstract
A novel technique of isochronous mass spectrometry (IMS), termed $B\rho$-defined IMS, was developed at the experimental cooler-storage ring CSRe in Lanzhou for the first time. Two time-of-flight detectors were installed in a straight section of the CSRe, thereby enabling simultaneous measurements of the velocity and revolution time of each stored short-lived ion. This technique boosts the broadband precision, efficiency, sensitivity, and accuracy of mass measurements of short-lived exotic nuclides. Using $B\rho$-defined IMS, the masses of ^{22}Al, ^{62}Ge, ^{64}As, ^{66}Se, and ^{70}Kr were measured for the first time, and the masses of ^{65}As, ^{67}Se, and other 21 nuclides were redetermined with improved accuracy. Mass data have been used in studies of relevant issues regarding nuclear structures and nuclear astrophysics. Herein, we review the development of experimental techniques and main physical results and outline plans for future experiments.

Keywords Nuclear mass · Storage ring · $B\rho$-defined isochronous · Nuclear structure · Nuclear astrophysics

1 Introduction

The mass of an atomic nucleus is a fundamental property that reflects the total energy of this quantum many-body system, which is composed of two types of fermions: protons and neutrons. Systematic and accurate knowledge of nuclear masses has wide applications in many areas of subatomic physics, ranging from nuclear structures to nuclear astrophysics and fundamental interactions and symmetries, depending on the mass precision achieved [1, 2]. For example, based on nuclear masses, well-known shell structure and pairing correlations were discovered in stable nuclei [3], and the disappearance of the magic neutron number $N = 20$ [4] and a new shell closure at $N = 32$ [5] were revealed in exotic neutron-rich nuclides. In addition to the mapping of the nuclear-mass surface [6–8], considerable attention has been paid to the precise mass measurements of exotic nuclei in specific mass regions, such as in the vicinity of doubly magic nuclei far from stability and the waiting-point nuclei in the rapid proton and rapid neutron capture processes.

Owing to more than a century of effort, the masses of approximately 2550 nuclides [9, 10] have been measured, as shown in Fig. 1. Currently, nuclides with unknown masses lie far from the valley of βstability, close to the borders of nuclear existence. Such nuclides are inevitably short-lived and have very low production yields, making their mass measurements extremely challenging. The performance of mass spectrometry of short-lived nuclei must improve in terms of sensitivity and precision.

Penning-trap mass spectrometry is widely used to deliver precise nuclear masses. Penning traps have produced numerous important results [11, 12]. However, in this application, a certain restriction threshold exists for the half-lives and/or production rates of the investigated nuclides. In recent years, multireflection time-of-flight spectrometry has emerged as a powerful technique for studying nuclei with short half-lives and low production rates [5, 13, 14]. However, in addition to the measurement time itself, applying these devices requires preparation steps such as cooling and bunching of low-energy radioactive species [15]. At high energies, mass spectrometers coupled directly to in-flight separators do not

Dedicated to Professor Wenqing Shen in honour of his 80th birthday.

✉ Meng Wang
wangm@impcas.ac.cn

✉ Yu-Hu Zhang
yhzhang@impcas.ac.cn

[1] CAS Key Laboratory of High Precision Nuclear Spectroscopy, Institute of Modern Physics, Chinese Academy of Sciences, Lanzhou 730000, China

[2] School of Nuclear Science and Technology, University of Chinese Academy of Sciences, Beijing 100049, China

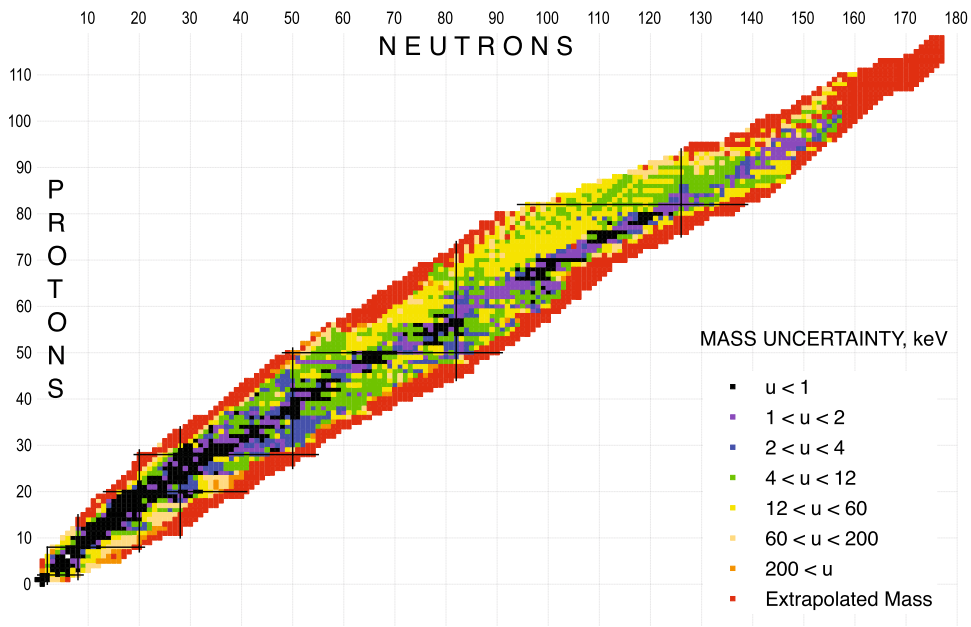

Fig. 1 (Color online) Nuclear chart displaying the mass-excess uncertainties in the latest atomic-mass evaluation AME2020 [10] for all nuclei in their ground state

require much time for ion preparation. Magnetic-rigidity time-of-flight ($B\rho$-TOF) mass spectrometry, implemented at radioactive-ion beamlines, has produced the masses of nuclides farthest away from the stability valley [16, 17], albeit with modest precision.

Isochronous mass spectrometry (IMS) in heavy-ion storage rings is an efficient and fast experimental technique [18] that is well suited for mass measurements of exotic nuclei with short lifetimes down to several tens of microseconds. Since the pioneering experiments conducted at the ESR in GSI, Darmstadt [19, 20], IMS has been established at the experimental cooler storage ring (CSRe) at the Institute of Modern Physics (IMP), Lanzhou [21, 22] and at the Rare RI Ring (R3) at the RIKEN Nishina Center in Wako/Japan [23].

IMS is typically used for mass measurements of heavy neutron-rich nuclides produced by the in-flight fission of uranium beams at the ESR [24, 25] and R3 [26–28]; see the review articles and references cited in [15, 29].

In the experiments, the isochronous mode of the storage ring was applied to achieve a relatively high resolving power for ions fulfilling the isochronous condition. However, for other ions that do not fulfill isochronicity, the mass resolution deteriorates rapidly. To improve the mass-resolving power over a broad m/q range, magnetic-rigidity tagging ($B\rho$-tagging) IMS was realized at the FRS-ESR facility at GSI [24, 30, 31] by inserting metal slits at the second dispersive focal plane of the FRS [32]. In the CSRe, an in-ring slit is used to restrict the magnetic-rigidity ($B\rho$) acceptance of the stored fragments [33]. However, both approaches have the significant limitation of losing transmission efficiency, which is not tolerable for mass measurements of exotic nuclei with very low production yields.

Recently, a new technique, termed $B\rho$-defined IMS, has been developed [34, 35], and a mass-resolving power of 1.3×10^5 (full width at half maximum; FWHM) can be achieved at the edges of the mass-to-charge ratio spectrum without losing any ions of interest [34]. Using this technique, the masses of ^{22}Al, ^{62}Ge, ^{64}As, ^{66}Se, and ^{70}Kr were measured for the first time, and the masses of ^{65}As, ^{67}Se, and other 21 nuclides were redetermined with improved accuracy. Based on these newly measured masses, investigations on different issues regarding nuclear structures and nuclear astrophysics based on these newly measured masses are also presented in this article.

2 $B\rho$-defined IMS

2.1 Principle

In conventional IMS, the ion-revolution times T_{exp} are measured using a single TOF detector [36, 37]. The mass-to-charge ratios of the ions, m/q, are derived according to [19, 20]:

$$\frac{m}{q} = \frac{B\rho}{\gamma v} = B\rho\sqrt{\frac{T_{\mathrm{exp}}^2}{C^2} - \frac{1}{v_{\mathrm{c}}^2}}, \tag{1}$$

where $B\rho$, v, γ, and C are the magnetic rigidity, velocity, Lorentz factor, and orbit length of the stored ions, respectively. v_{c} is the speed of light. $B\rho$ and C are assumed to be the same for all ions, and the masses of aimed ions can be deduced using ions with known masses as calibrants.

In real experiments, the momentum acceptance of the storage ring should be considered, and the dispersed $B\rho$ and C of the stored ions should follow the $B\rho(C)$ function. The relative slope of $B\rho(C)$

$$\frac{\Delta B\rho/B\rho}{\Delta C/C} = \gamma_t^2, \tag{2}$$

introduces a new quantity, γ_t, called the transition point of the storage ring [38]. γ_t is determined solely by the machine lattice settings and is independent of the ion species.

Owing to the momentum dispersion of the stored ions, the variation in the revolution times is as follows:

$$\frac{\Delta T_{exp}}{T_{exp}} = \frac{\Delta C}{C} - \frac{\Delta v}{v} = \left(\frac{1}{\gamma_t^2} - \frac{1}{\gamma^2}\right)\frac{\Delta B\rho}{B\rho}. \tag{3}$$

In the experiments, the storage ring was tuned to be isochronous, that is, $\gamma \sim \gamma_t$, for the ions of interest, and a high mass-resolving power could be achieved in a small region of the m/q spectrum. For other ions with $\gamma \neq \gamma_t$, the mass-resolving power decreased rapidly.

To further reduce the influence of momentum dispersion and achieve broadband high mass-resolving power, two TOF detectors are installed in one of the straight sections of the ring such that both the revolution times T_{exp} and velocities v_{exp} of the stored ions [39] can be measured simultaneously. Consequently, the orbital length of each ion $C_{exp} = T_{exp} \times v_{exp}$ can be deduced directly.

Using ions with known masses as calibrants, a one-to-one correspondence of $B\rho \sim C$ is obtained, providing more information on the momentum dispersion. By fitting the $B\rho \sim C$ data, we obtain the $B\rho_{fit}(C_{exp})$ function, and the m/q value of any ion can be deduced from the fitted function as follows:

$$\frac{m}{q} = \frac{B\rho_{fit}(C_{exp})}{(\gamma v)_{exp}}. \tag{4}$$

In the simulations, the uncertainties of m/q values are mainly due to the uncertainties of the velocity measurements and instability of γ_t [40–42]. A data-analysis method was developed to achieve $B\rho$-defined IMS at the storage ring CSRe in Lanzhou.

2.2 Technique details

The experiments were conducted at the accelerator complex of the IMP in Lanzhou, China. The nuclides of interest were produced by fragmenting the primary beams at a speed of $> 0.7 \times v_c$ on $10 \sim 15$ mm ^{9}Be production targets. The produced nuclides were selected using the in-flight fragment separator, the second Radioactive Isotope Beam Line in Lanzhou (RIBLL2) [43]. They were then injected into and stored in the CSRe.

Figure 2 presents a schematic of the CSRe with the three TOF detectors noted in this figure. The detector TOF0 was used in the conventional IMS. The detectors TOF1 and TOF2 were used in $B\rho$-defined IMS. Each detector consists of a thin carbon foil ($\phi = 40$ mm, 18 μg/cm^2 thick) and a set of microchannel plates (MCP) [36, 37].

When an ion passes through the carbon foil, secondary electrons are released from the foil surface and guided to the MCP by perpendicularly arranged electric and magnetic fields. Compared to the previous detector TOF0, the electric-field strengths in TOF1 and TOF2 increased from 130 to 180 V/mm to improve the time resolution of the detector, as shown in Fig. 3a. A time resolution of 18.5 ± 2 ps was achieved in the offline tests of TOF1 and TOF2 [37]. Fast timing signals from the two MCPs were recorded using a single oscilloscope to avoid the jitter effects of two or more electronic instruments [45]. The sampling rate was set to 50 GHz.

To achieve $B\rho$-defined IMS, a new isochronous mode setting was specially designed at the CSRe [44]. Figure 3b shows the dispersion function $D_x = \frac{x}{\Delta p/p}$ as a function of the longitudinal position s of the CSRe. The dispersion function at the detector positions was designed to be close to 0 m for a high transition efficiency of the ions owing to the limited size of the carbon foils ($\phi = 40$ mm). To ensure the accuracy of the detector installation, a calibration system using a short-pulsed ultraviolet laser was also applied at the CSRe [46].

In real experiments, γ_t is not constant for all orbit lengths owing to high-order magnetic fields from imperfect

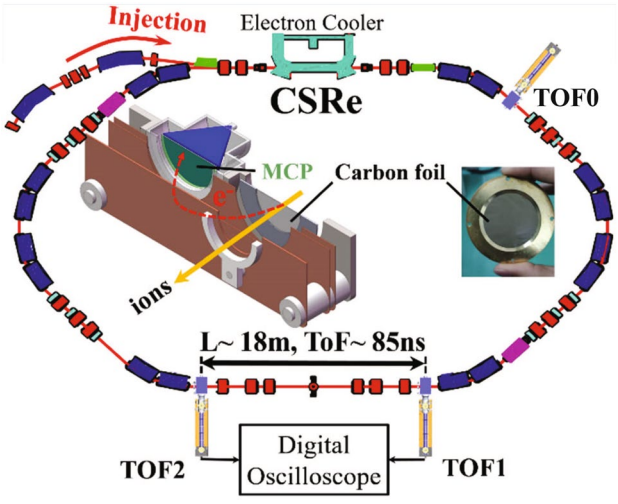

Fig. 2 (Color online) Schematic of CSRe with the arrangement of three TOF detectors [34]

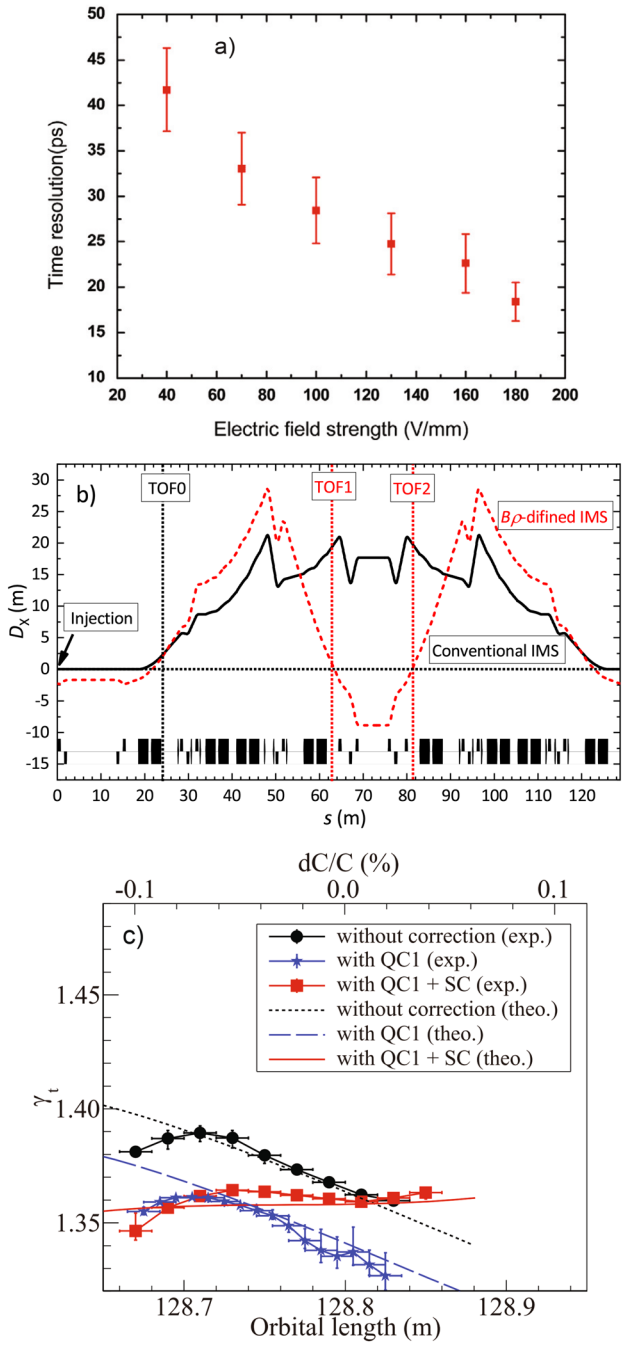

Fig. 3 (Color online) **a** Time resolution of the TOF detector as a function of the electric-field strength. [37]. **b** Dispersion functions used in conventional IMS (black solid line) and $B\rho$-defined IMS (red dashed line) as a function of the longitudinal position s of CSRe [44]. The positions of the three TOF detectors are denoted using dotted lines. **c** The transition energy γ_t as a function of orbital length due to isochronous corrections of quadrupole magnets and sextupole magnets [44]

storage-ring facilities [44, 47, 48]. A minor modification of the quadrupole and sextupole fields was performed to reduce the variation in γ_t as a function of the orbit length C [44],

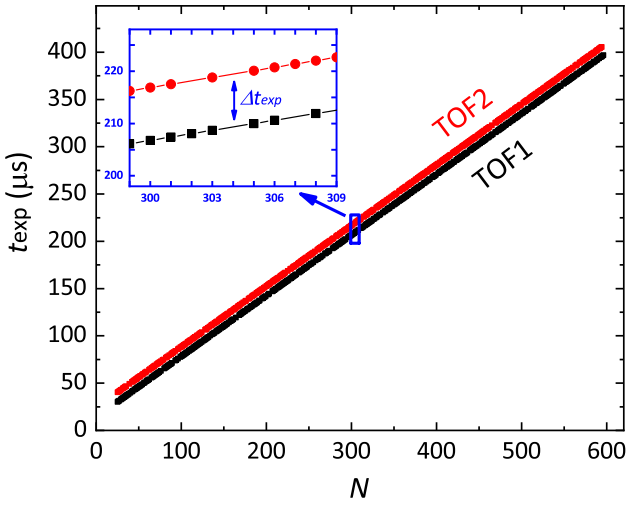

Fig. 4 (Color online) The passage times t_{exp} of a single $^{45}V^{23+}$ measured by detectors TOF1 and TOF2 as a function of the revolution number N [39]. For illustration purposes, the time stamps from TOF2 are shifted upwards by 10 μs. The inset illustrates an enlarged region at $299 \le N \le 309$ showing the missing time stamps in some revolutions. The error bar of each data point is within the symbol size

as shown in Fig 3c. However, the variation in γ_t within the momentum acceptance cannot be eliminated completely in a real experiment. The residual nonlinear effects in the $\gamma_t(C)$ curve should be considered in data analysis.

2.3 Velocity measurement of stored ions

Figure 4 shows the passage times t_{exp} of a single $^{45}V^{23+}$ ion as a function of revolution number N for TOF1 and TOF2 [39]. The slope $\partial t_{exp}/\partial N$ is the revolution time T_{exp}, and the distance between the two curves is the time of flight (TOF) Δt_{exp} between the two detectors. The mean velocity of an ion circulating in the ring v is obtained by

$$v = \frac{L}{\Delta t_{exp} - \Delta t_d}, \tag{5}$$

where L is the distance between the two TOF detectors in the straight section of the CSRe and $\Delta t_d = t_d^{TOF2} - t_d^{TOF1}$ is the time-delay difference between the two timing signals transmitted from the detectors to the oscilloscope. The values of L and Δt_d were measured in a dedicated study using a laser-calibration system [46] and were redetermined in each experiment using stored ions with known masses as calibrants [35]. The precise velocity measurement of a stored ion critically depends on the precision determination of Δt_{exp} between TOF1 and TOF2.

Data analyses of conventional IMS usually show that the flight time of an ion is a smooth function of the revolution number. Considering the energy loss in a thin carbon

foil, $t_{exp}(N)$ can be described by a third-order polynomial function:

$$t_{fit}(N) = a_0 + a_1 \times N + a_2 \times N^2 + a_3 \times N^3. \quad (6)$$

In addition, the influence of the betatron oscillations of the ions should be considered [39], and the fit function of $t_{exp}(N)$ curves should be modified as follows:

$$\begin{aligned} t_{fit}(N) = {} & a_0 + a_1 \times N + a_2 \times N^2 + a_3 \times N^3 \\ & + A_x \times [2\pi(Q_{x0} \times N + Q_{x1} \times N^2) + \phi_x] \\ & + A_y \times [2\pi(Q_{y0} \times N + Q_{y1} \times N^2) + \phi_y]. \end{aligned} \quad (7)$$

The polynomial function in Eq. (7) describes ion motion with a mean orbital length, whereas the sinelike terms describe the periodic time fluctuations owing to betatron oscillations.

A straightforward method to deduce Δt_{exp} is to use the existing coincident timestamps from both TOF detectors in the same revolution. Alternatively, a fitting procedure using Eq. (6) and Eq. (7) has been performed, and Fig. 5 shows the average uncertainties of Δt_{exp} as a function of the atomic number Z using these three methods.

The smallest mean value of $\sigma(\Delta t_{exp})$ has been obtained using Eq. (7). This indicates that considering and addressing the effects of betatron oscillations can significantly improve the precision of the Δt_{exp} values as well as the ion velocities. The mean uncertainties exhibited a decreasing trend from lighter to heavier ions. This can be understood if the Z-dependence of the detection efficiency of the detectors is considered; that is, a higher detection efficiency yields lower statistical errors in Δt_{exp}. The lowest mean uncertainties of Δt_{exp} were within the range of 2.0 − 6.4 ps, corresponding to a relative precision of $(2.2 - 7.2) \times 10^{-5}$ with respect to the average TOF between the two TOF detectors of $\Delta t_{exp} \approx 89$ ns. Compared with the momentum acceptance ±0.2% of the CSRe [49], the precision of Δt_{exp} is sufficient for new IMS development.

2.4 Determination of mass values

Using ions with known masses and the measured revolution times T_{exp} and velocities v_{exp}, the magnetic rigidity $B\rho_{exp} = m/q \times (\gamma v)_{exp}$ and orbit length $C_{exp} = T_{exp} \times v_{exp}$ can be easily extracted. Figure 6 shows a scatterplot of $B\rho_{exp}$ versus C_{exp} [34, 35].

For an ideal storage ring with a completely constant γ_t within the momentum acceptance, the one-to-one correspondence of $B\rho \sim C$ should follow the simple form:

$$B\rho(C) = B\rho_0 \left(\frac{C}{C_0}\right)^{\gamma_t^2}, \quad (8)$$

where $B\rho_0$ and C_0 are reference parameters.

In real experiments, the nonlinear effects in the $\gamma_t(C)$ curve shown in Fig. 3c should be considered. Because these residual nonlinear effects may differ in each experiment, Eq. (8) is modified by including additional terms. For example,

$$B\rho(C) = B\rho_0 \left(\frac{C}{C_0}\right)^{K} + a_1 e^{-a_2(C-C_0)} \quad (9)$$

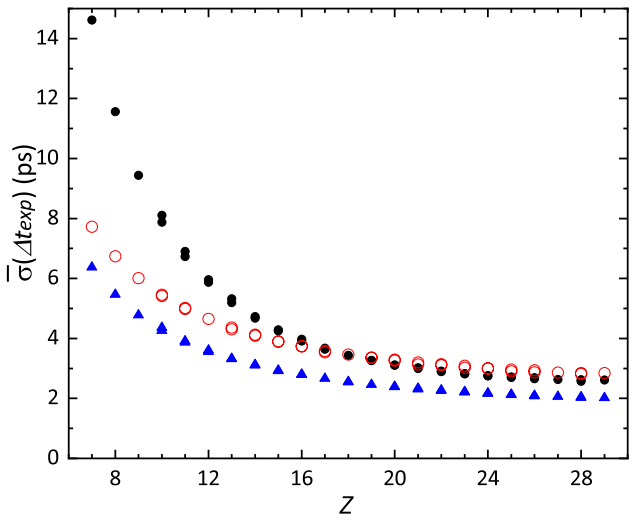

Fig. 5 (Color online) Average uncertainty of Δt_{exp} as a function of atomic number Z, extracted from coincident time stamps (black filled circles) and by using the third-order polynomial fit function with [Eq. (7)] (blue filled triangles) and without [Eq. (6)] (red opened circles) the sinelike terms

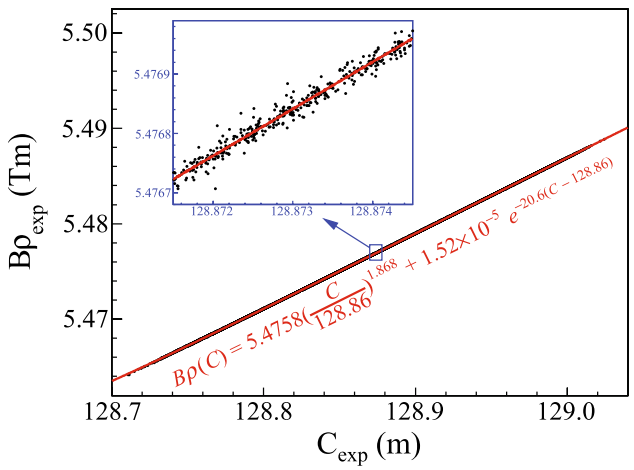

Fig. 6 (Color online) Plot of $B\rho_{exp}$ versus C_{exp} with the fit results (solid line) [35]. The fitted expression is noted in this figure

was used in the experiments described in Refs. [34, 35]. The fit result of Eq. (9) is shown in Fig. 6. The m/q spectrum was deduced from the fitted results.

The instability of magnetic fields is one of the most significant challenges in precision mass measurements at the CSRe storage ring. Over the past decade, extensive efforts have been dedicated to both hardware improvements [50] and data-analysis enhancements [51, 52], aimed at mitigating the impact of magnetic-field drift. Using data from the two TOF detectors, we developed a more precise correction method [35].

The changes in the dipole magnetic fields led to vertical drifts in the measured $B\rho(C)$ curve. This phenomenon can be clearly observed in Fig. 7a, where the fit residuals $B\rho^i_{\rm exp} - B\rho(C^i_{\rm exp})$ are presented as functions of the injection number. To achieve the high mass-resolving power, the originally determined quantities $\{C^i_{\rm exp}, T^i_{\rm exp}, v^i_{\rm exp}, i = 1, 2, ..., N_s\}$ need to be corrected to $\{C^i_{\rm cor}, T^i_{\rm cor}, v^i_{\rm cor}, i = 1, 2, ..., N_s\}$ corresponding to a reference magnetic-field setting with B_0 assuming the magnetic field is stable. To obtain the latter, $C^i_{\rm exp} = C^i_{\rm cor}$ must be confined (equivalent to a common radius $\rho^i_{\rm exp} = \rho^i_{\rm cor}$). Consequently, the magnetic rigidity and velocity of each ion in the same injection are scaled by a constant ratio:

$$B\rho^i_{\rm cor} = \frac{1}{R_M} B\rho^i_{\rm exp} \text{ or } (\gamma v)^i_{\rm cor} = \frac{1}{R_M} (\gamma v)^i_{\rm exp}, \tag{10}$$

where

$$R_M = \left(\frac{B}{B_0}\right)_{\rm CSRe} = \left(\frac{B\rho^i_{\rm exp}}{B\rho(C^i_{\rm exp})}\right)_{\rm ion}. \tag{11}$$

The ratio R_M can be deduced from the experimental data of reference ions with known masses for each injection. Figure 7b shows that the fitted residuals after correction produce $B\rho^i_{\rm cor} - B\rho(C^i_{\rm exp})$ as a function of the injection number. The slow variations in the magnetic-field drifts were almost completely removed. After the field-drift correction, the obtained values $\{B\rho^i_{\rm cor}, v^i_{\rm cor}, C^i_{\rm exp}\}$ are available for all ion species. Their m/q values were then calculated from the $B\rho_{\rm cor} \sim C_{\rm exp}$ curve, using Eq. (4) following the same procedure as that shown in Fig. 6.

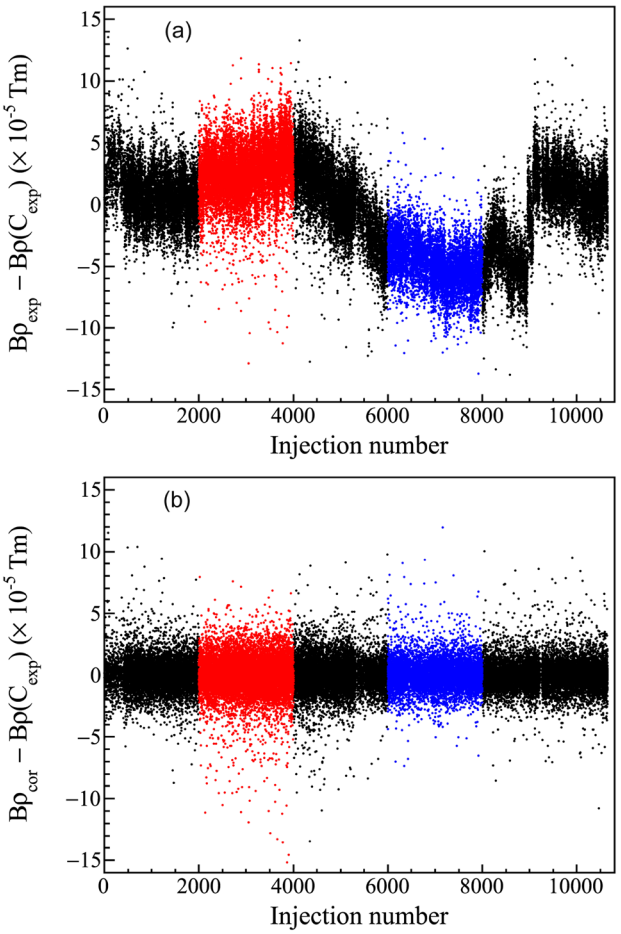

Fig. 7 (Color online) **a** Scatter plot of fit residuals, $B\rho^i_{\rm exp} - B\rho(C^i_{\rm exp})$, as a function of injection number illustrating slow variations of the magnetic fields of the CSRe [35]. **b** Similar to (**a**), but with the corrected $B\rho_{\rm cor}$

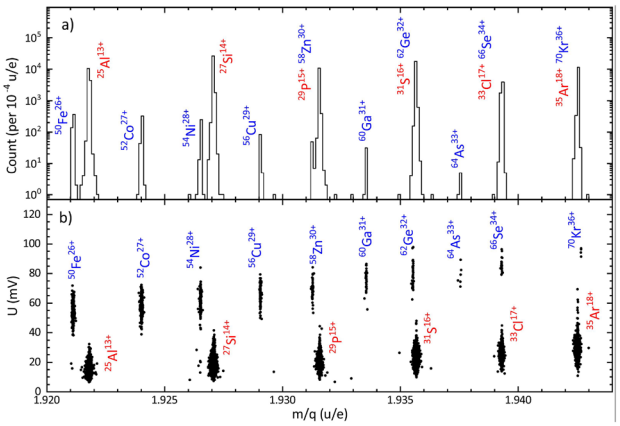

Fig. 8 **a** Part of the m/q spectrum and **b** the corresponding scatter plot of U versus m/q in Ref. [53]. The ion species are also indicated. Note that the unresolved ^{62}Ge^{32+}, ^{66}Se^{34+}, and ^{70}Kr^{36+} in the m/q spectrum are completely separated from ^{31}S^{16+}, ^{33}Cl^{37+}, and ^{35}Ar^{18+}, respectively, in the plot of U versus m/q

2.5 Improvements compared with the conventional IMS

Figure 8 shows part of the m/q spectrum of Ref. [53]. The peaks of the nuclei with nearly identical m/q ratios may overlap. To obtain the m/q values from the overlapping peaks, we introduce a Z-dependent parameter, $U = \varepsilon\bar{H}$, extracted from the timing signals of the TOF detectors [54, 55]. Here, ε is the detection efficiency for a specific ion and $\bar{H}$ is the average signal amplitude of that ion.

To demonstrate the increasing resolving power of the new approach compared to the conventional IMS, we transformed the m/q spectrum into a new revolution-time spectrum [34, 35], T_{fix}, at a fixed magnetic rigidity $B\rho_{\mathrm{fix}} = 5.4758$ Tm (the corresponding orbit length is $C_{\mathrm{fix}} = 128.86$ m), as follows:

$$T_{\mathrm{fix}} = C_{\mathrm{fix}}\sqrt{\frac{1}{(B\rho)^2_{\mathrm{fix}}}\left(\frac{m}{q}\right)^2 + \left(\frac{1}{v_c}\right)^2}. \quad (12)$$

For example, scatter plots of T_{exp} and T_{fix} versus C_{exp} for $^{24}\mathrm{Al}^{13+}$ ions are shown in Fig. 9 [34, 35].

Clearly, the two states in ^{24}Al, separated by a mass difference of 425.8(1) keV [9], cannot be resolved in the T_{exp} spectrum, whereas the two peaks can be separated in the T_{fix} spectrum. The standard deviations of the T peaks derived from the corresponding spectra are shown in Fig. 10.

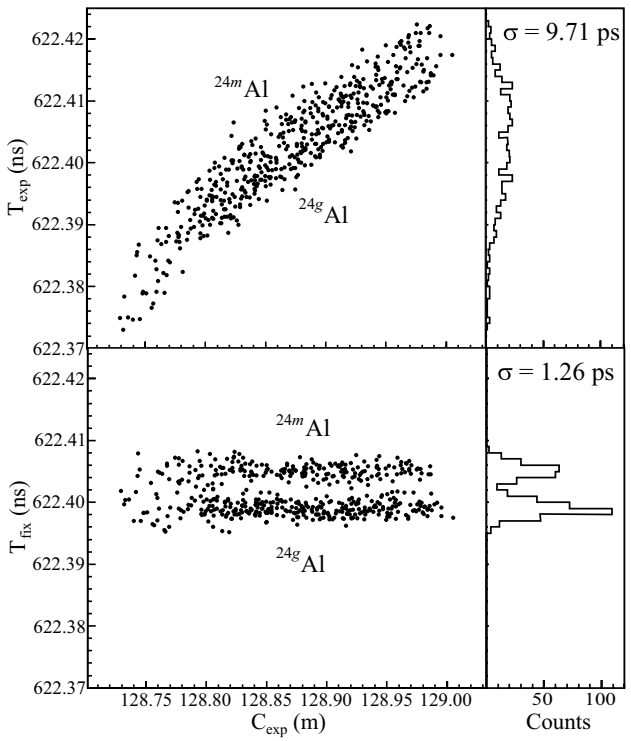

Fig. 9 Scatter plots of T_{exp} and T_{fix} versus C_{exp} for $^{24}\mathrm{Al}^{13+}$ ions [34, 35]

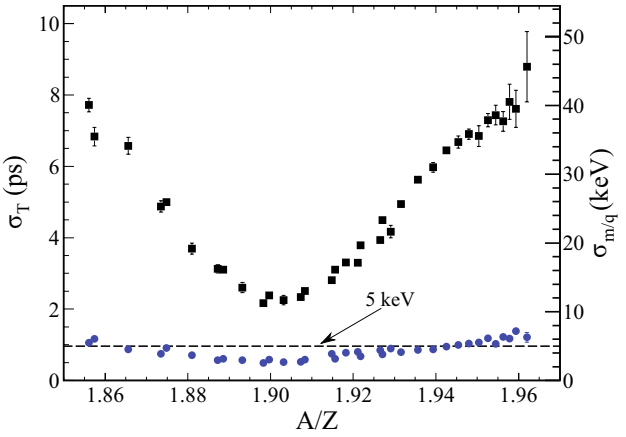

Fig. 10 Standard deviations of the T peaks (left scale) derived from the original revolution-time spectrum (black filled squares) and from the newly constructed spectrum (blue circles). The corresponding absolute accuracies of mass-to-charge ratios are given on the right scale. [34, 35]

The standard deviations, σ_{T}, of the T peaks in the original T_{exp} spectrum exhibit a parabolic dependence on m/q. σ_{T} approaches a minimum at approximately 2 ps for a limited number of nuclides (isochronicity window). In the spectrum obtained using the new $B\rho$-defined IMS technique, $\sigma_T = 0.5$ ps was achieved in the isochronicity window, corresponding to a mass-resolving power of 3.3×10^5 (FWHM). At the edges of the spectrum, a mass-resolving power of 1.3×10^5 (FWHM) can be achieved, which is an improvement by a factor of approximately 8 compared to the conventional method. We emphasize that this was done without reducing the $B\rho$ acceptance of either the ring or transfer line. The right scale in Fig. 10 shows the corresponding absolute m/q precision. We emphasize that an m/q precision of 5 keV is obtained for a single stored ion.

Using the $T_z = -1/2$ nuclides to calibrate the spectrum, the redetermined masses of the $T_z = -1$ nuclides are compared with well-known literature values in Fig. 11 [35]. The results obtained using T_{exp} as in conventional IMS are shown in Fig. 11a, where the systematic deviations for the $T_z = -1$ nuclides can be clearly observed. Such systematic deviations are caused mainly by the different momentum distributions and energy losses of the two series of nuclides with $T_z = -1/2$ and -1 [49]. Not only did the statistical uncertainties significantly decrease, but the systematic deviations demonstrated in Fig. 11a are completely removed over a wide range of revolution times.

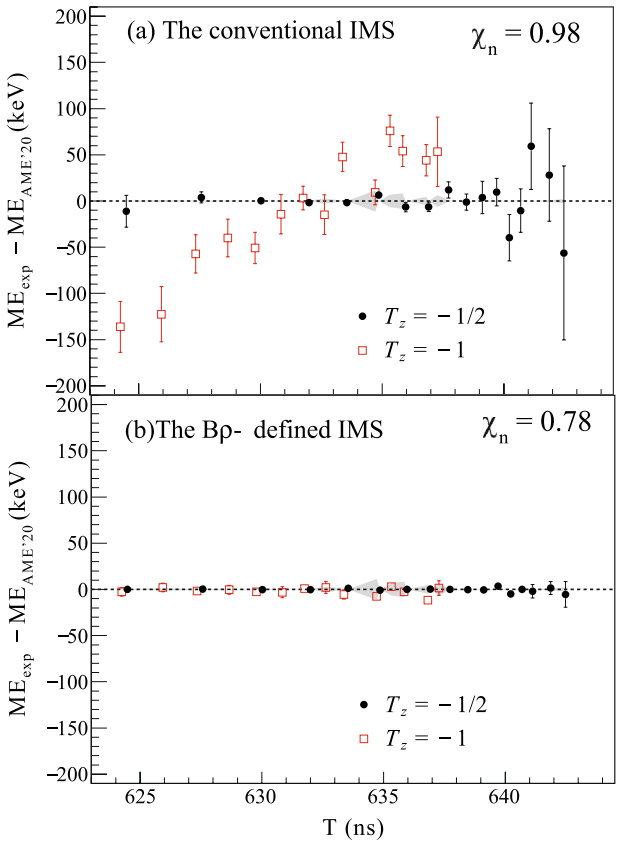

Fig. 11 Comparison of redetermined mass excesses of $T_z = -1$ nuclides (filled red squares), deduced from **a** T_{exp} and **b** T_{fix}, with literature values [9] using the $T_z = -1/2$ nuclides (filled black circles) as calibrants. Masses are determined from the revolution-time spectrum following the procedures described in [56] and χ_n is the normalized chi-square for the reference nuclides used in the calibration [34, 35]

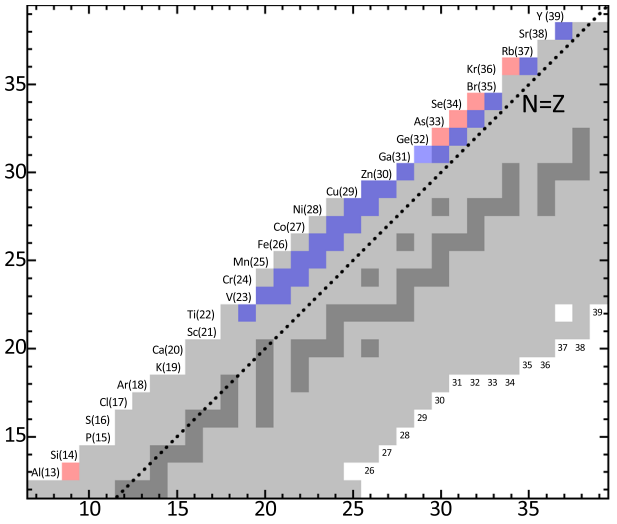

Fig. 12 (Color online) Partial chart of nuclides. Stable nuclides are shown in black. Nuclides with known masses in AME2020 [9] are shown in gray. The nuclei whose masses were measured for the first time are indicated in red. Blue represents the remeasured nuclei with improved precision

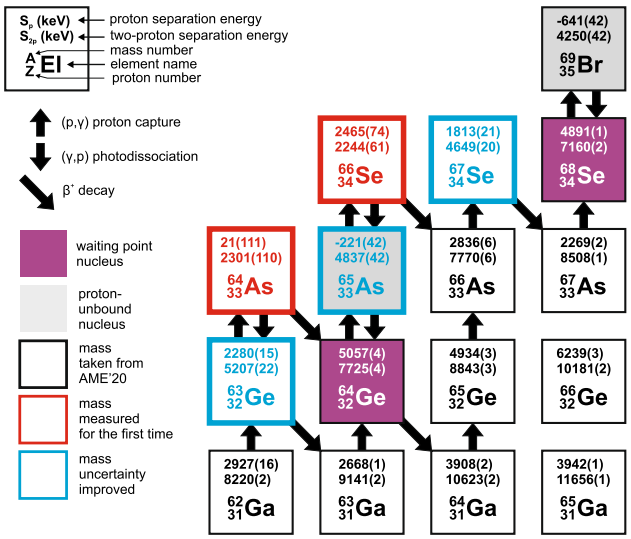

Fig. 13 Nuclear chart around the *rp*-process waiting point ^{64}Ge [57]. Nuclides whose masses were obtained from AME2020 [9], whose masses were experimentally determined, or whose mass uncertainties were improved in Ref. [57] are indicated with black, red, and blue, respectively. The one- (S_p) and two-proton (S_{2p}) separation energies (values expressed in keV) follow the same color code. The pathway of *rp*-process nucleosynthesis is shown with black arrows. Refer to the legend for more details

3 Recent results

Several experiments on $B\rho$-defined IMS using ^{58}Ni, ^{86}Kr, ^{78}Kr, and ^{36}Ar as primary beams were performed. Some newly determined masses have also been reported [34, 35, 53, 57, 58]. Analysis of the data on neutron-rich ^{86}Kr fragments and part of the data on neutron-deficient ^{36}Ar fragments is still in progress. Figure 12 summarizes the published results in the chart of nuclides. The masses of five short-lived neutron-deficient nuclides were measured for the first time, and 23 nuclides were remeasured with higher precision. In the following section, we discuss the application of our measurements to the study of nuclear astrophysics and nuclear structures.

3.1 GS 1826-24 X-ray burst and neutron stars

Type-I X-ray bursts occur on the surfaces of neutron stars, accreting hydrogen- and helium-rich matter from companion stars in a stellar binary system [59]. The burst is powered by a sequence of nuclear reactions, termed the rapid-proton-capture nucleosynthesis process (*rp* process) [60], which is a sequence of proton captures, and β decays along the proton

drip line. Figure 13 shows a nuclear chart around the *rp*-process waiting point ^{64}Ge. Measurements of neutron-deficient ^{78}Kr projectile fragments at the CSRe provided the masses for ^{63}Ge, ^{64,65}As, and ^{66,67}Se using $B\rho$-defined IMS, and all the relevant separation energies around the waiting point ^{64}Ge were determined [57].

The impact of these new masses was investigated using state-of-the-art multizone X-ray burst simulations. Simulated X-ray burst light curves are shown in Fig. 14. The new nuclear masses, particularly the less-bound ^{65}As and more-bound ^{66}Se, result in a stalled *rp*-process at the ^{64}Ge waiting point. The new distributions of the elements produced through the *rp*-nucleosynthesis ("ashes") are also modified, as shown in the inset of Fig. 14. The ash abundances of Urca nuclides are particularly notable [66, 67]. A 17% increase in the $A = 64$ ash mass fraction results in increased electron-capture heating, and a 14% decrease in the $A = 65$ ash mass fraction resulted in reduced Urca cooling, implying a somewhat warmer accreted neutron-star crust.

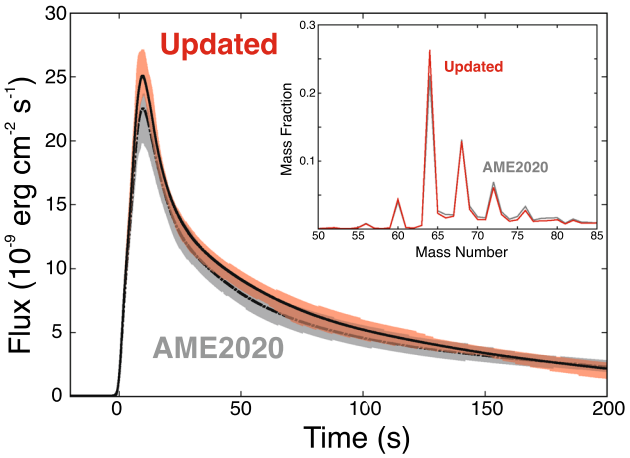

Fig. 14 (Color online) Calculated X-ray-burst light curves [57]. The baseline nuclear-physics input is labeled as AME2020 (dashed-dotted line and gray band). The result including the nuclear masses determined in Ref. [57] is marked as Updated (solid-line and red band). The light-curve bands correspond to 68% confidence intervals. The inset shows the calculated mass fractions $X(A)$ as a function of mass number

The X-ray-burst luminosity measured by a telescope is directly proportional to the emitted light flux and inversely proportional to the square of the distance d^2 and surface gravitational redshift $(1+z)^2$ of the burst corrected by the electromagnetic-wave transport efficiency [68–70]. Our new light curve enables the setting of new constraints on the optimal d and $(1+z)$ parameters that fit the observational data [57]. The results are presented in Fig. 15a. The increased peak luminosity requires distance d to be increased by ~0.4 kpc from approximately 5.8 kpc to approximately 6.2 kpc. The *rp*-process stalled at ^{64}Ge leads to extended hydrogen burning in the light curve, thereby extending the burst tail. Consequently, the modeled light curve must be less time-dilated, thereby reducing $(1+z)$.

The constraints on $(1+z)$ can be further converted into limits on the neutron-star compactness $(M_{\rm NS}/R_{\rm NS})$ following the approach introduced in [71]. The general relativistic neutron-star mass $M_{\rm GR}$ and radius $R_{\rm GR}$ are determined using $(1+z) = 1/\sqrt{1-2GM_{\rm GR}/(R_{\rm GR}v_c^2)}$, where G is the gravitational constant. If the Newtonian mass is equal to the general

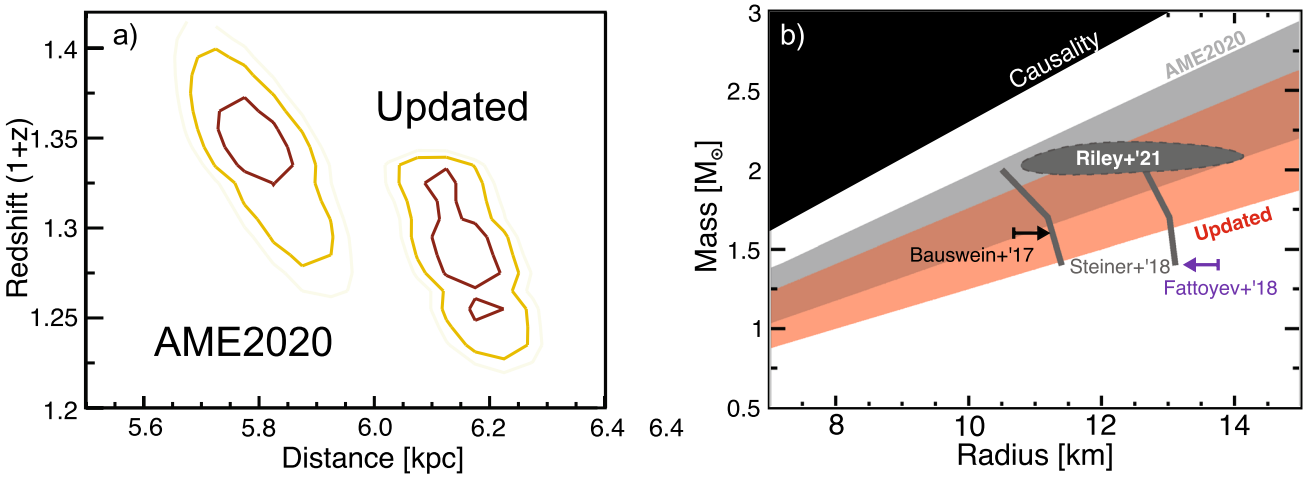

Fig. 15 (Color online) **a** Surface gravitational redshift versus the distance of the source GS 1826-24 obtained through a comparison of the modeled light curves shown in Fig. 14 and the observational data from the year 2007 bursting epoch [57]. The colors indicate 68% (red), 90% (yellow), and 95% (gray) confidence intervals. Two regions correspond to results using previously known masses (AME2020) and those including our new masses (Updated). **b** Neutron-star mass $(M_{\rm NS})$ versus radius $(R_{\rm NS})$ constraints calculated from the $(1+z)$ 95% confidence intervals shown in (**a**) [57]. Limits for neutron-star compactness determined using other astrophysical observables [61–65] are also shown in this figure

relativistic mass $M_{\rm NS} = M_{\rm GR}$, then $R_{\rm GR} = \sqrt{(1+z)}R_{\rm NS}$. The compactness constraints corresponding to the 95% confidence intervals shown in Fig. 15a are shown in Fig. 15b along with the mass and radius constraints from other observational probes and theoretical limits.

Recently, the newly determined compactness $\xi = M_{\rm NS}/R_{\rm NS}$ was incorporated into a comprehensive Bayesian statistical framework to investigate its impact on the equation of state (EOS) of supradense neutron-rich matter and the spin frequency required for GW 190814's minor m_2 with mass $2.59 \pm 0.05\ M_\odot$ to be a rotationally stable pulsar. The EOS of high-density symmetric nuclear matter must be softened significantly, while the symmetry energy at supersaturation densities is stiffened compared to our prior knowledge from earlier analyses using data from both astrophysical observations and terrestrial nuclear experiments [72, 73].

3.2 Thermonuclear reaction rate of ^{57}Cu$(p,\gamma)^{58}$Zn in the *rp* process

In addition to research around the waiting-point ^{64}Ge, the newly determined mass of the neutron-deficient nuclide ^{58}Zn was used to re-evaluate the thermonuclear rate of the ^{57}Cu$(p,\gamma)^{58}$Zn reaction around the waiting-point ^{56}Ni [74]. The re-evaluated thermonuclear rate was higher than the most recently published rate by a factor of up to three in the temperature range of $0.2\ {\rm GK} \le T \le 1.5\ {\rm GK}$. One-zone post-processing type-I X-ray-burst calculations were performed. Figure 16 shows the fractional difference in abundance as a function of mass number. The updated rate and new mass of ^{58}Zn resulted in noticeable abundance variations for nuclei with $A = 56 - 59$ and a reduction in $A = 57$ abundance by up to 20.7%.

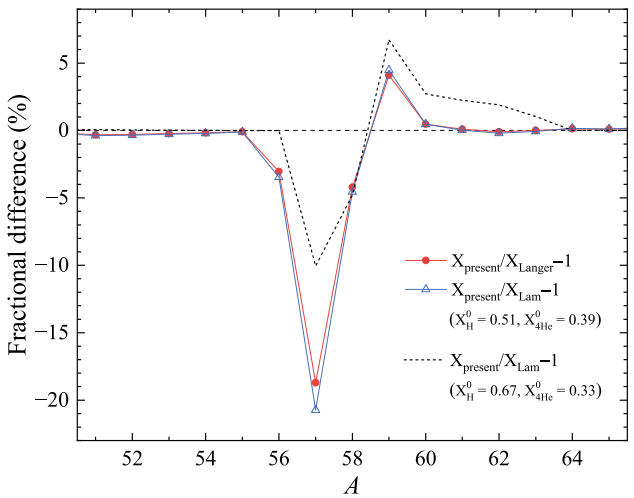

Fig. 16 Fractional difference of abundance by mass number of Ref. [74] (present) compared to those using the Langer et al. rate [75] (red filled circles) and Lam et al. [70] rates (blue open triangles). The black dashed line represents the result with initial mass fractions [76]

3.3 Residual proton–neutron interactions in the $N = Z$ nuclei

The binding energy of a nucleus, $B(Z, N)$, is derived directly from the atomic masses and embodies the sum of the overall interactions inside the nucleus. Binding-energy differences can isolate specific classes of interactions and provide insights into nuclear structural modifications [1, 15]. An important mass filter, the double binding-energy difference denoted as $\delta V_{\rm pn}$, has been used to isolate the residual proton–neutron (pn) interactions [77–79] and to sensitively probe a variety of structure phenomena, such as the onset of collectivity and deformation [80–83], changes to the underlying shell structure [84], and phase-transitional behavior [81, 85]. Conventionally, $\delta V_{\rm pn}$ values are derived as follows [79]:

$$\delta V_{\rm pn}^{\rm ee}(Z,N) = \frac{1}{4}\big[B(Z,N) - B(Z,N-2) - B(Z-2,N) + B(Z-2,N-2)\big], \tag{13}$$

$$\delta V_{pn}^{\rm oo}(Z,N) = \big[B(Z,N) - B(Z,N-1) - B(Z-1,N) + B(Z-1,N-1)\big], \tag{14}$$

$$\delta V_{\rm pn}^{\rm oe}(Z,N) = \frac{1}{2}\big[B(Z,N) - B(Z,N-2) - B(Z-1,N) + B(Z-1,N-2)\big], \tag{15}$$

$$\delta V_{\rm pn}^{\rm eo}(Z,N) = \frac{1}{2}\big[B(Z,N) - B(Z,N-1) - B(Z-2,N) + B(Z-2,N-1)\big], \tag{16}$$

and are termed the empirical residual proton–neutron interactions. Equations (13)–(16) are suitable for nuclei with (Z, N) =even–even, odd–even, even–odd, and odd–odd, respectively.

Measurements of neutron-deficient ^{78}Kr projectile fragments at the CSRe provided masses for ^{58}Zn, ^{60}Ga, ^{62}Ge, ^{64}As, ^{66}Se, and ^{70}Kr $T_z = -1$ nuclides as well as ^{61}Ga, ^{63}Ge, ^{65}As, ^{67}Se, ^{71}Kr, and ^{75}Sr $T_z = -1$ nuclides [53]. The newly measured masses provide the $\delta V_{\rm pn}$ values using Eq. (13) for nuclei with $N = Z =$ even ($\delta V_{\rm pn}^{\rm ee}$) and Eq. (14) for nuclei with $N = Z =$ odd ($\delta V_{\rm pn}^{\rm oo}$). The results are presented in Fig. 17a together with the $\delta V_{\rm pn}$ values extracted using the currently available mass models [86–94].

Our results show that an increasing trend in $\delta V_{\rm pn}^{\rm oo}$ beyond $Z = 28$ (red dashed line) is established, which has been suggested as an indication of the restoration of the

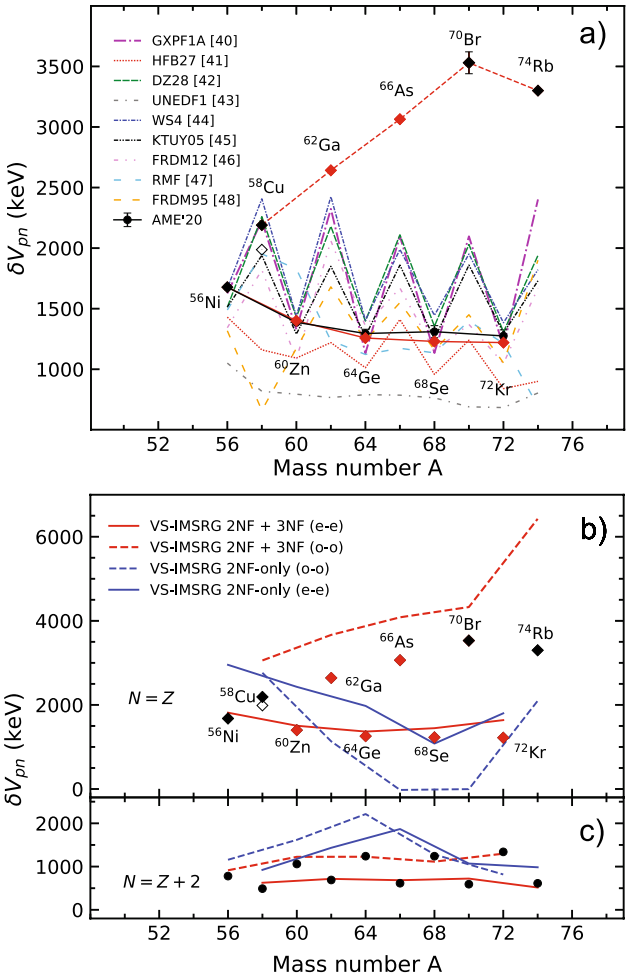

Fig. 17 **a** Experimental $\delta V_{\rm pn}$ for $N = Z$ nuclei beyond $A = 56$ and comparison with different mass-model predictions [86–94]. Red lines are included to guide the eye. Red symbols indicate that one of the new masses in Ref. [53] was used. $\delta V_{\rm pn}$ of ^{58}Cu using the binding energy of the $T = 1, J^{\pi} = 0^{+}$ excited state [9] is marked with open diamond shapes. ME(^{70}Br) = −52030(80) keV is obtained from [95, 96]. $\delta V_{\rm pn}$ values obtained using the extrapolated masses in AME2020 [9, 9] are connected by the black solid line. **b** and **c** show experimental $\delta V_{\rm pn}$ values for $N = Z$ and $N = Z + 2$ nuclei beyond $A = 56$ together with the *ab initio* calculations [53]. Data uncertainties are within the size of the symbols. $\delta V_{\rm pn}$ values from *ab initio* calculations using 2NF+3NF and 2NF only are plotted as red and blue lines (solid lines for even–even and dashed lines for odd–odd), respectively

pseudo-SU(4) symmetry in the *fp* shell [97, 98]. $\delta V_{\rm pn}^{\rm ee}$ follows a decreasing trend (red solid line), as reported in the lower-mass region [78, 99]. This contrary to the expectation of pseudo-SU(4) symmetry [79, 100]. We extracted the $\delta V_{\rm pn}$ values using the predicted masses of frequently used mass models [86–94] and observed that none of the models can reproduce the bifurcation of $\delta V_{\rm pn}$ (see Fig. 17a).

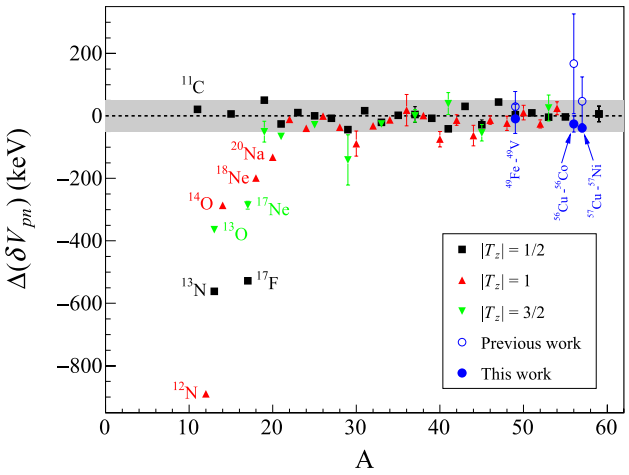

Fig. 18 (Color online) Differences of $\delta V_{\rm pn}$ for mirror nuclei [35]. The gray shadow indicates an error band of 50 keV. The neutron-deficient partners are indicated for the mirror pairs with $A \leq 20$

To understand the bifurcation of δV_{pn}, we performed an *ab initio* valence-space in-medium similarity renormalization group (VS-IMSRG) calculation using a chiral interaction with a two-nucleon force (2NF) at N^{3}LO and a three-nucleon force (3NF) at N^{2}LO, named EM1.8/2.0 [101].

As shown in Fig. 17c, our calculations with 3NF excellently reproduced the experimental $\delta V_{\rm pn}$ with $N = Z + 2$ nuclei, demonstrating the capability of the *ab initio* approach. For $N = Z$ nuclei, the calculations reproduced the $\delta V_{\rm pn}^{\rm ee}$ data from ^{56}Ni to ^{72}Kr, which decreased marginally with increasing A. As both $T = 0$ and $T = 1$ pn correlations are naturally included in the *ab initio* calculation, reasonable agreement with the experimental $\delta V_{\rm pn}^{\rm oo}$ values is also obtained from ^{58}Cu to ^{70}Br. In particular, the increasing trend of $\delta V_{\rm pn}^{\rm oo}$ with changing A is well reproduced.

Recently, a shell-model-like approach based on relativistic density-functional theory was established [102] by simultaneously treating the neutron–neutron, proton–neutron, and proton–proton pairing correlations both microscopically and self-consistently. The calculated $\delta V_{\rm pn}$ values reproduced the observed bifurcation in Fig. 17 well. The mechanism for this abnormal bifurcation was owing to the enhanced proton–neutron pairing correlations in the odd–odd $N = Z$ nuclei compared with the even–even ones.

3.4 Mirror symmetry of residual proton–neutron interactions

In addition to the $\delta V_{\rm pn}$ of $N = Z$ nuclei, mirror symmetry of the residual *p*–*n* interactions on both sides of the $Z = N$ line [56] was observed. Such mirror symmetry was observed

many years ago by Jänecke [103] and was recently used by Zong et al. [104] to make high-precision mass predictions for neutron-deficient nuclei.

Figure 18 shows the energy differences were defined as $\Delta(\delta V_{\rm pn}) = \delta V_{\rm pn}(T_z^<, A) - \delta V_{\rm pn}(T_z^>, A)$ [35]. Here, $T_z^</T_z^>$ represents the negative/positive value of T_z for the mirror nuclei. The $\delta V_{\rm pn}$ values are calculated using Eqs. (13)–(16), using mass data from AME2020 [9]. Masses of ^{49}Fe and ^{55}Cu $T_z = -3/2$ nuclides as well as ^{54}Ni $T_z = -1$ deduced from measurements of neutron-deficient ^{58}Ni projectile fragments at the CSRe are also used in these calculations, as shown by the blue dots.

$\Delta(\delta V_{\rm pn})$ values scatter around zero within an error band of ±50 keV for the $A > 20$ mirror pairs, indicating that the mirror symmetry of $\delta V_{\rm pn}$ holds well in this mass region. Notably, the mass of ^{55}Cu was redetermined with significantly improved precision, and its value was 172 keV more bound than the previous value [105]. Using this new mass, the calculated $\delta V_{\rm pn}$ value of ^{56}Cu was approximately equal to that of ^{56}Co. Consequently, $\Delta(\delta V_{\rm pn}) = \delta V_{\rm pn}(^{56}{\rm Cu}) - \delta V_{\rm pn}(^{56}{\rm Co})$ fits general systematics well with a high level of accuracy (see Fig. 18). This result further confirmed the reliability of the new mass value for ^{55}Cu.

In the lighter-mass region with $A \leq 20$, the so-called mirror symmetry of $\delta V_{\rm pn}$ is broken into a few mirror pairs (see Fig. 18). That is, the $\delta V_{\rm pn}$ values of the neutron-deficient nuclei are systematically smaller than those of the corresponding neutron-rich partners. Such mirror-symmetry breaking is simply attributed to the binding-energy effect [103]. Here, we note that one of the four nuclei is particle-unbound, which may lead to the mirror-symmetry breaking of $\delta V_{\rm pn}$. Thus, the mirror symmetry of $\delta V_{\rm pn}$ cannot be used to predict masses with $A \leq 20$.

3.5 Ground-state mass of ^{22}Al and test of *ab initio* calculations

The level structure of mirror nuclei is commonly addressed and discussed based on the isospin symmetry, which is a basic assumption in the fields of particle and nuclear physics. However, this symmetry is approximate and the corresponding deviation is called isospin symmetry breaking (ISB) [106–110]. Studies on mirror nuclei offer profound insights into the origin of ISB and further information about nuclear structures, as well as facilitate the evaluation of nuclear models [106–113]. A key quantity in the investigation of ISB in mirror nuclei is the mirror-energy difference (MED) [106, 114, 115], which is defined as follows:

$$MED = E_x(J, T, T_z = -T) - E_x(J, T, T_z = T), \quad (17)$$

where $E_x(J, T, T_z)$ denotes the excitation energy of a state with spin J, isospin T, and z-projection T_z.

^{22}Al is the lightest-bound Al isotope with $T_z = -2$. Two low-lying 1^+ states in odd–odd ^{22}Al were identified via β-delayed one-proton emissions from ^{22}Si [112]. However, their excitation energies have not been determined precisely because of the lack of an experimental ground-state mass of ^{22}Al. Recently, the ground-state mass excess of ^{22}Al was measured for the first time using $B\rho$-defined IMS as 18103(10) keV [58], which is 97(400) keV smaller than the extrapolated ME = 18200(400) keV in AME2020 [9]. The new mass excess value allowed the determination of the excitation energies of the two low-lying states, $E_x(1_1^+) = 1002(51)$ keV and $E_x(1_2^+) = 2242(51)$ keV in ^{22}Al, with a significantly reduced uncertainty of 51 keV. The experimental MEDs of $1_{1,2}^+$ states in ^{22}Al-^{22}F mirror nuclei are shown in Fig. 19 [58].

The MEDs of ^{22}Al-^{22}F mirror nuclei were calculated using an *ab initio* VS-IMSRG approach, employing several sets of nuclear forces derived from chiral effective-field theory [58]. The large uncertainties in the MEDs obtained in Ref. [112] prevented the benchmarking of the theoretical calculations. The uncertainties of the MEDs obtained in this study are significantly reduced, and the results show that the MED of the 1_1^+ states is larger than that of the 1_2^+ states in ^{22}Al-^{22}F mirror nuclei. Based on the *ab initio* calculations, we observe that the MEDs calculated with 1.8/2.0(EM), NNLO$_{opt}$, and $NN + 3N$(lnl) interactions are in good agreement with the experimental data, especially the result from NNLO$_{opt}$, whereas the predicted MED values with NNLO$_{sat}$ for the $1_{1,2}^+$ states are inverted when compared with the experimental data. Therefore, the MED of the mirror nuclei serves as a more sensitive observable tool for testing theoretical calculations when comparing the excitation

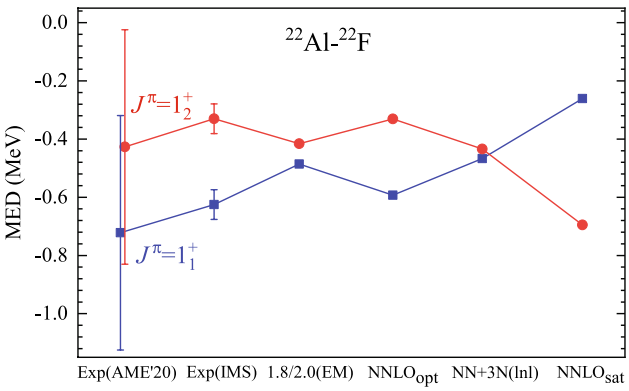

Fig. 19 (color online) MEDs of the $1_{1,2}^+$ states in ^{22}Al/^{22}F mirror nuclei by employing *ab initio* VS-IMSRG calculations with four sets of nuclear interactions. The experimental MED values are plotted with error bars, whereas the calculated values are not

spectra. Moreover, mirror systems ^{22}Al-^{22}F were investigated using the *ab initio* Gamow shell model based on the same EM1.8/2.0 interaction [116]. Within the Gamow shell-model calculations, the effective Hamiltonian is derived through many-body perturbation theory, and continuum coupling is well accounted for using the Berggren basis. The results obtained from *ab initio* GSM calculations were consistent with those obtained from the VS-IMSRG calculations based on the EM1.8/2.0 interaction.

3.6 Test of isospin multiplet mass equation

The mass of a set of isobaric analog states (IASs) can be described by the well-known quadratic isospin multiplet mass equation (IMME) [117]:

$$ME(A,T,T_z) = a(A,T) + b(A,T) \times T_z + c(A,T) \times T_z^2, \quad (18)$$

where the MEs are the mass excesses of the IASs of a multiplet with a fixed mass number A and total isospin T. T is equal to or greater than the projection of T, $T_z = (N-Z)/2$, for a specific nucleus. The coefficients a, b, and c depend on A, T, and other quantum numbers, such as spin and parity J^π, but are independent of T_z. The quadratic form of the IMME, that is, Eq. (18), is commonly considered accurate within uncertainties of a few tens of keV. In this context, precise mass measurements can be used to test its validity (see Ref. [118] and references therein). Typically, we add extra terms to Eq. (18) such as dT_z^3 and/or eT_z^4, which provide a measure of the breakdown of the quadratic form of the IMME. Numerous measurements were performed to investigate the validity of the IMME. Reviews and compilations of existing data can be found in Refs. [119, 120] and the references cited therein.

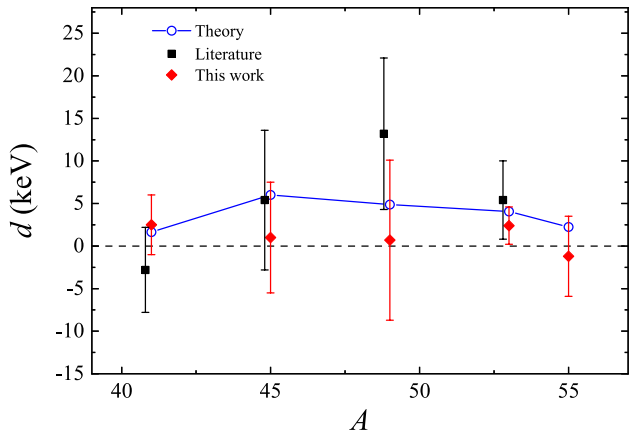

Fig. 20 d coefficients of the cubic form of IMME for the $T = 3/2$, $A = 41$, 45, 49, 53, and 55 isospin quartets [35]. The solid line connects the predicted d values from theoretical calculations [121]

Measurements of neutron-deficient ^{58}Ni projectile fragments at the CSRe provided the masses for ^{41}Ti, ^{45}Cr, ^{49}Fe, ^{53}Ni, and ^{55}Cu using $B\rho$-defined IMS [35]. Using these new masses, the four experimental masses of the $T = 3/2$ IASs were completed; thus, the validity of the quadratic form of the IMME could be tested, reaching the heaviest $A = 55$ isospin quartet. The mass data were fitted to the cubic form of the IMME by adding the dT_z^3 term to Eq. (18), and the fitted d coefficients are shown in Fig. 20.

Compared with previous results in Ref. [118], we conclude that the trend of a gradual increase in d with A in the *fp* shell [118] was not confirmed, at least at the present level of accuracy. Given that all the extracted d coefficients are compatible with zero, the quadratic form of the IMME is valid for the cases investigated here. Figure 20 shows the d values obtained from the theoretical calculations [121]. The predicted nonzero d coefficients for these $T = 3/2$ isospin quartets cannot be discarded owing to large experimental uncertainties.

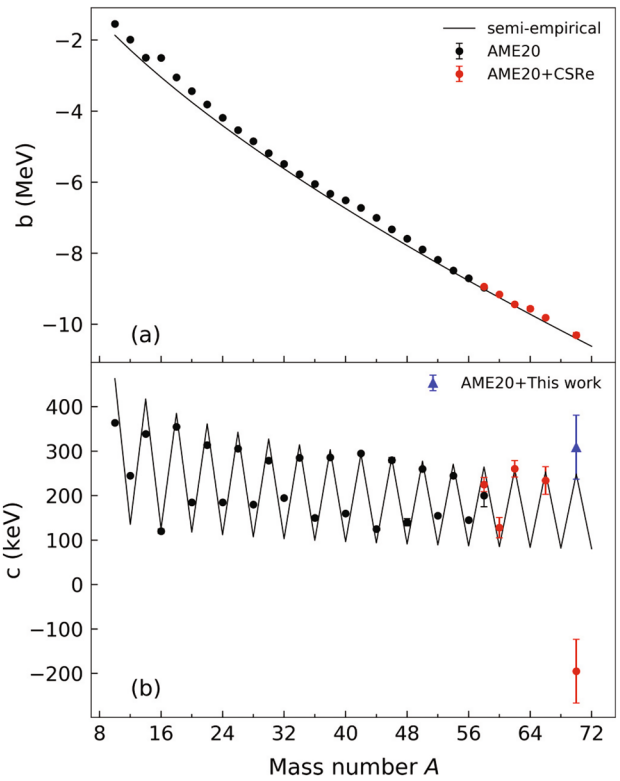

Fig. 21 b and c coefficients of the quadratic IMME [122] extracted using the AME2020 mass data [9] (black circles) and the new masses from the CSRe [53] (red circles). The c coefficient using ME(^{70}Br) = −51934(16) keV is indicated by the blue triangle [122]. The solid lines denote a semiempirical formula. Refer to details in Ref. [122]

3.7 Ground-state mass of ^{70}Br

The masses of the $T_z = -1$ nuclides ^{58}Zn, ^{60}Ga, ^{62}Ge, ^{64}As, ^{66}Se, and ^{70}Kr deduced from measurements of neutron-deficient ^{78}Kr projectile fragments at the CSRe are used to investigate the systematics of b and c coefficients of the quadratic form of the IMME up to the upper fp-shell nuclei [122].

Using the new mass results reported in Ref. [53] and the literature values in the latest atomic-mass evaluation (AME2020) [9], the b and c coefficients are deduced according to Eqs. (18) up to $A = 70$, as shown in Fig. 21 [122].

Figure 21a shows that the deduced b coefficients follow the smooth trend established in the lighter-mass region. The obtained c coefficients exhibit regular zig-zag staggering with changes in A, as shown in Fig. 21b. However, the regular staggering trend breaks at $A = 70$ and the derived c coefficient becomes negative. This anomaly was analyzed and attributed to the presently adopted mass of ^{70}Br in the latest atomic-mass evaluation (AME2020).

The smooth trend of the b coefficients and the regular staggering pattern of the c coefficients can be deduced using the mass formula given in Ref. [123] for the members of an isobaric multiplet characterized by A, T, and T_z:

$$M(A,T,T_z) = M_0(A,T) + E_c(A,T,T_z) + T_z \times \Delta m_{nH}, \quad (19)$$

where $E_c(A,T,T_z)$ represents the total charge-dependent energy in the nucleus and Δm_{nH} is the neutron–hydrogen mass difference. The semi-classical approach [124, 125],

$$E_c = \left\{0.6Z^2 - 0.46Z^{4/3} - 0.15[1-(-1)^Z]\right\}\frac{e^2}{r_0 A^{1/3}}, \quad (20)$$

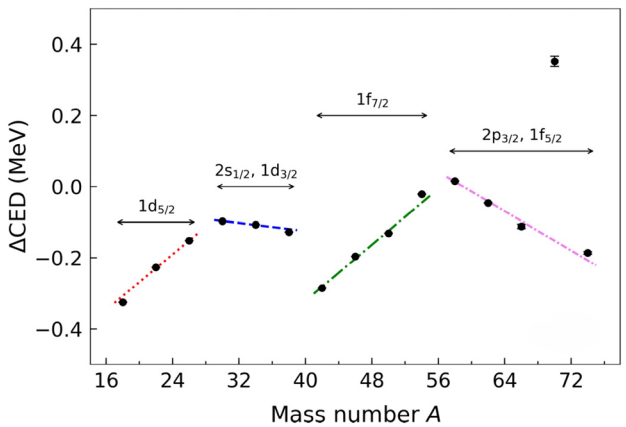

Fig. 22 Plot of $\Delta\text{CED} = \text{CED}_{exp} - \text{CED}_{th}$ and the least-squares fits with linear functions [122]. $\Delta\text{CED} = -152(16)$ keV at $A = 70$ is thereby deduced. Data uncertainties are within the size of the symbols. Orbits for major shells and subshells are indicated

can be used to calculate the theoretical values of parameters b, c. The calculated b and c coefficients are shown in Fig. 21 as solid lines.

As reported in Refs. [126, 127], a combination of the theoretical calculations of Coulomb-energy differences (CEDs) and experimental masses of neutron-rich nuclei provides reliable masses for proton-rich nuclei. The CED between the $T_z = 0$ and $T_z = +1$ isobaric pairs was extracted using

$$\text{CED} = M(A, T_z = 0) - M(A, T_z = +1) + \Delta m_{nH}. \quad (21)$$

Figure 22 shows the CDE difference $\Delta\text{CED} = \text{CED}_{exp} - \text{CED}_{th}$ as a function of the mass number A [122].

The ΔCEDs follow very good linear behavior within each shell closure, while exhibiting a large deviation at $A = 70$ between $A = 58$ and $A = 74$.

Under the assumption of a smooth variation in the CED with changing mass number A, the ground-state mass excess of ^{70}Br is deduced to be −51934(16) keV, which is 508(22) keV more bound than the adopted value [122]. Using the new ME of ^{70}Br, the recalculated c coefficient is obtained using Eq. (18), and the results are shown in Fig. 21b. The new c coefficient now fits well into the systematics and is consistent with a simple theoretical estimate. This supports our recommended ME value of ^{70}Br obtained from the systematics of the Coulomb-energy differences.

4 Summary and outlook

In summary, significantly improved isochronous mass spectrometry, the $B\rho$-defined IMS, has been pioneered at the experimental cooler-storage ring CSRe. Owing to the simultaneous measurement of the revolution time and velocity of every stored short-lived ion, the sensitivity and precision of the mass measurements significantly increased. The time sequences of the two TOF detectors were unique for each ion. Only a few tens of signals were sufficient for unambiguous ion identification. This unparalleled property of the $B\rho$-defined IMS makes it, in principle, a background-free technique. The overall measurement time was less than 1 ms, indicating that all β-decaying nuclei could be studied without lifetime restrictions. High mass-resolving power was achieved over the entire $B\rho$ acceptance of the storage ring, implying that a large range of m/q values can be covered in a single-machine setting. This is a remarkable achievement, which indicates that the storage of a single short-lived ($T_{1/2} \geq 100$ μs) ion is sufficient for mass determination with $\approx 5q$ keV precision. Thus, $B\rho$-defined IMS is an ideal technique for high-precision mass measurements of the most

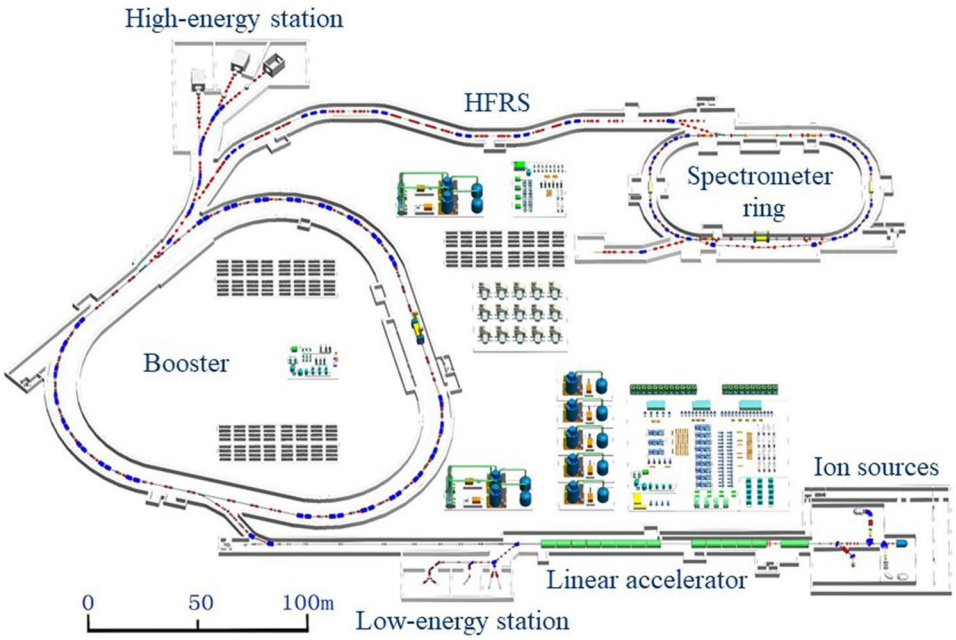

Fig. 23 Layout of HIAF [128]. The major sub-systems are sketched, including the ion sources, superconducting ion linear accelerator, high-energy synchrotron booster, high-energy fragment separator, and experimental spectrometer ring. The low-energy and high-energy experimental stations are also indicated

exotic nuclides, which have the shortest half-lives and lowest production yields.

Using $B\rho$-defined IMS, the masses of ^{22}Al, ^{62}Ge, ^{64}As, ^{66}Se, and ^{70}Kr were measured for the first time, and the masses of ^{41}Ti, ^{43}V, ^{45}Cr, ^{47}Mn, ^{49}Fe, ^{51}Co, ^{53}Ni, ^{55}Cu, ^{44}V, ^{46}Cr, ^{48}Mn, ^{50}Fe, ^{52}Co, ^{54}Ni, ^{56}Cu, ^{58}Zn, ^{60}Ga, ^{61}Ga, ^{63}Ge, ^{66}As, ^{67}Se, ^{71}Kr, and ^{75}Sr were re-determined with improved accuracy. Given these newly determined masses, interesting issues in nuclear astrophysics and nuclear structures have been investigated.

The merits of the novel IMS are demonstrated by the considerably increased sensitivity and accuracy of its measurements. A spectrometer ring (SRing) [129] at the high-intensity heavy-ion accelerator facility (HIAF) [128, 130, 131] is under construction, as shown in Fig. 23. $B\rho$-defined IMS is planned for application in the SRing, and the distance between the two TOF detectors in the straight section will be ~39 m, which is ~2.0 times the distance in the CSRe. Assuming that the time resolution of the TOF detectors is the same as that used in the CSRe, in principle, the precision of the velocity measurement would be increased by a factor of approximately 2.0, and the mass precision would be further improved. Two isochronous mode settings with $\gamma_t = 1.43, 1.67$ were designed for the mass-measurement experiments in the SRing. In the future, both neutron-deficient and neutron-rich nuclei will be covered in experiments at the SRing.

Acknowledgements This work is supported in part by the National Key R&D Program of China (Grant No. 2023YFA1606401), CAS Project for Young Scientists in Basic Research (Grant No. YSBR-002), Strategic Priority Research Program of the Chinese Academy of Sciences (Grant No. XDB34000000), and NSFC (Grant No. 12305126). X.L.Y. acknowledges the support from the Young Scholar of Regional Development, CAS (Grant No.[2023]15). Y.M.X. acknowledges the support from the Youth Innovation Promotion Association of the Chinese Academy of Sciences (Grant No. 2021419).

References

1. K. Blaum, High-accuracy mass spectrometry with stored ions. Phys. Rep. **425**, 1–78 (2006). https://doi.org/10.1016/j.physrep.2005.10.011
2. D. Lunney, J.M. Pearson, C. Thibault, Recent trends in the determination of nuclear masses. Rev. Mod. Phys. **75**, 1021–1082 (2003). https://doi.org/10.1103/RevModPhys.75.1021
3. A.N. Bohr, B.R. Mottelson, *Nuclear Structure*, vol. 2 (World Scientific Publishing Company, Singapore, 1998)
4. C. Thibault, R. Klapisch, C. Rigaud et al., Direct measurement of the masses of ^{11}Li and $^{26-32}$Na with an on-line mass spectrometer. Phys. Rev. C **12**, 644–657 (1975). https://doi.org/10.1103/PhysRevC.12.644
5. F. Wienholtz, D. Beck, K. Blaum et al., Masses of exotic calcium isotopes pin down nuclear forces. Nature **498**, 346–349 (2013). https://doi.org/10.1038/nature12226
6. T. Radon, H. Geissel, G. Münzenberg et al., Schottky mass measurements of stored and cooled neutron-deficient projectile fragments in the element range of 57≤Z≤84. Nucl. Phys. A **677**, 75–99 (2000). https://doi.org/10.1016/S0375-9474(00)00304-3
7. Y. Novikov, F. Attallah, F. Bosch et al., Mass mapping of a new area of neutron-deficient suburanium nuclides. Nucl. Phys. A **697**, 92–106 (2002). https://doi.org/10.1016/S0375-9474(01)01233-7
8. J. Van Schelt, D. Lascar, G. Savard et al., First results from the CARIBU facility: mass measurements on the *r*-process path. Phys. Rev. Lett. **111**, 061102 (2013). https://doi.org/10.1103/PhysRevLett.111.061102
9. M. Wang, W. Huang, F. Kondev et al., The AME 2020 atomic mass evaluation (II). Tables, graphs and references*. Chin. Phys. C **45**, 030003 (2021). https://doi.org/10.1088/1674-1137/abddaf

10. F. Kondev, M. Wang, W. Huang et al., The NUBASE2020 evaluation of nuclear physics properties. Chin. Phys. C **45**, 030001 (2021). https://doi.org/10.1088/1674-1137/abddae
11. T. Eronen, A. Kankainen, J. Äystö, Ion traps in nuclear physics-recent results and achievements. Prog. Part. Nucl. Phys. **91**, 259–293 (2016). https://doi.org/10.1016/j.ppnp.2016.08.001
12. J. Dilling, K. Blaum, M. Brodeur et al., Penning-trap mass measurements in atomic and nuclear physics. Ann. Rev. Nucl. Part. Sci. **68**, 45–74 (2018). https://doi.org/10.1146/annurev-nucl-102711-094939
13. M. Mougeot, D. Atanasov, J. Karthein et al., Mass measurements of $^{99-101}$In challenge ab initio nuclear theory of the nuclide ^{100}Sn. Nat. Phys. **17**, 1099–1103 (2021). https://doi.org/10.1038/s41567-021-01326-9
14. S. Beck, B. Kootte, I. Dedes et al., Mass measurements of neutron-deficient Yb isotopes and nuclear structure at the extreme proton-rich side of the $N = 82$ shell. Phys. Rev. Lett. **127**, 112501 (2021). https://doi.org/10.1103/PhysRevLett.127.112501
15. T. Yamaguchi, H. Koura, Y. Litvinov et al., Masses of exotic nuclei. Prog. Part. Nucl. Phys. **120**, 103882 (2021). https://doi.org/10.1016/j.ppnp.2021.103882
16. Z. Meisel, S. George, S. Ahn et al., Nuclear mass measurements map the structure of atomic nuclei and accreting neutron stars. Phys. Rev. C **101**, 052801 (2020). https://doi.org/10.1103/PhysRevC.101.052801
17. S. Michimasa, M. Kobayashi, Y. Kiyokawa et al., Mapping of a new deformation region around ^{62}Ti. Phys. Rev. Lett. **125**, 122501 (2020). https://doi.org/10.1103/PhysRevLett.125.122501
18. Y.H. Zhang, Y.A. Litvinov, T. Uesaka et al., Storage ring mass spectrometry for nuclear structure and astrophysics research. Physica Scripta **91**, 073002 (2016). https://doi.org/10.1088/0031-8949/91/7/073002
19. M. Hausmann, F. Attallah, K. Beckert et al., First isochronous mass spectrometry at the experimental storage ring ESR. Nucl. Inst. Methods Phys. Res. Sect. A Accel. Spectromet. Detect. Assoc. Equip. **446**, 569–580 (2000). https://doi.org/10.1016/S0168-9002(99)01192-4
20. J. Stadlmann, M. Hausmann, F. Attallah et al., Direct mass measurement of bare short-lived ^{44}V, ^{48}Mn, ^{41}Ti and ^{45}Cr ions with isochronous mass spectrometry. Phys. Lett. B **586**, 27–33 (2004). https://doi.org/10.1016/j.physletb.2004.02.014
21. H.S. Xu, Y.H. Zhang, Y.A. Litvinov, Accurate mass measurements of exotic nuclei with the CSRe in Lanzhou. Int. J. Mass Spectrom. **349–350**, 162–171 (2013). https://doi.org/10.1016/j.ijms.2013.04.029
22. M.Z. Sun, X.H. Zhou, M. Wang et al., Precision mass measurements of short-lived nuclides at HIRFL-CSR in lanzhou. Front. Phys. **13**, 132112 (2018). https://doi.org/10.1007/s11467-018-0844-5
23. D. Nagae, S. Omika, Y. Abe et al., First demonstration of mass measurements for exotic nuclei using Rare-RI Ring. JPS Conf. Proc. **35**, 011014 (2021). https://doi.org/10.7566/JPSCP.35.011014
24. B. Sun, R. Knöbel, Y. Litvinov et al., Nuclear structure studies of short-lived neutron-rich nuclei with the novel large-scale isochronous mass spectrometry at the FRS-ESR facility. Nucl. Phys. A **812**, 1–12 (2008). https://doi.org/10.1016/j.nuclphysa.2008.08.013
25. R. Knöbel, M. Diwisch, H. Geissel et al., New results from isochronous mass measurements of neutron-rich uranium fission fragments with the FRS-ESR-facility at GSI. Eur. Phys. J. A **52**, 138 (2016). https://doi.org/10.1140/epja/i2016-16138-6
26. H.F. Li, S. Naimi, T.M. Sprouse et al., First application of mass measurements with the Rare-RI Ring reveals the solar *r*-process abundance trend at $A = 122$ and $A = 123$. Phys. Rev. Lett. **128**, 152701 (2022). https://doi.org/10.1103/PhysRevLett.128.152701
27. S. Naimi, Y. Yamaguchi, T. Yamaguchi et al., Recent achievements at the Rare-RI Ring, a unique mass spectrometer at the RIBF/RIKEN. Eur. Phys. J. A **59**, 90 (2023). https://doi.org/10.1140/epja/s10050-023-01009-4
28. D. Nagae, S. Omika, Y. Abe et al., Isochronous mass spectrometry at the riken rare-ri ring facility. Phys. Rev. C **110**, 014310 (2024). https://doi.org/10.1103/PhysRevC.110.014310
29. B. Franzke, H. Geissel, G. Münzenberg, Mass and lifetime measurements of exotic nuclei in storage rings. Mass Spectrom. Rev. **27**, 428–469 (2008). https://doi.org/10.1002/mas.20173
30. H. Geissel, Y.A. Litvinov, Precision experiments with relativistic exotic nuclei at GSI. J. Phys. G Nucl. Part. Phys. **31**, S1779–S1783 (2005). https://doi.org/10.1088/0954-3899/31/10/072
31. H. Geissel, R. Knöbel, Y.A. Litvinov et al., A new experimental approach for isochronous mass measurements of short-lived exotic nuclei with the FRS-ESR facility. Hyperfine Interact. **173**, 49–54 (2006). https://doi.org/10.1007/s10751-007-9541-4
32. H. Geissel, G. Munzenberg, K. Riisager, Secondary exotic nuclear beams. Ann. Rev. Nucl. Part. Sci. **45**, 163–203 (1995). https://doi.org/10.1146/annurev.ns.45.120195.001115
33. J. Liu, X. Xu, P. Zhang et al., Improving the resolving power of Isochronous Mass Spectrometry by employing an in-ring mechanical slit. Nuc. Inst. Methods Phys. Res. Sect. B:Beam Interact. Mater. Atoms **463**, 138–142 (2020). https://doi.org/10.1016/j.nimb.2019.06.007
34. M. Wang, M. Zhang, X. Zhou et al., Bρ-defined isochronous mass spectrometry: an approach for high-precision mass measurements of short-lived nuclei. Phys. Rev. C **106**, L051301 (2022). https://doi.org/10.1103/PhysRevC.106.L051301
35. M. Zhang, X. Zhou, M. Wang et al., *B*ρ-defined isochronous mass spectrometry and mass measurements of ^{58}Ni fragments. Eur. Phys. J. A **59**, 27 (2023). https://doi.org/10.1140/epja/s10050-023-00928-6
36. B. Mei, X. Lin Tu, M. Wang et al., A high performance Time-of-Flight detector applied to isochronous mass measurement at CSRe. Nucl. Inst. Methods Phys. Res. Sect. A Accel. Mass Spectrom. Detect. Assoc. Equip. **624**, 109–113 (2010). https://doi.org/10.1016/j.nima.2010.09.001
37. W. Zhang, X.L. Tu, M. Wang et al., Time-of-flight detectors with improved timing performance for isochronous mass measurements at the CSRe. Nucl. Inst. Methods Phys. Res. Sect. A Accel. Spectrom. Detect. Assoc. Equip. **756**, 1–5 (2014). https://doi.org/10.1016/j.nima.2014.04.051
38. S.Y. Lee, *Accelerator Physics* (World Scientific Publishing Company, Singapore, 2018). https://doi.org/10.1142/11111
39. X. Zhou, M. Zhang, M. Wang et al., In-ring velocity measurement for isochronous mass spectrometry. Phys. Rev. Accel. Beams **24**, 042802 (2021). https://doi.org/10.1103/PhysRevAccelBeams.24.042802
40. R.J. Chen, Y.J. Yuan, M. Wang et al., Simulations of the isochronous mass spectrometry at the HIRFL-CSR. Physica Scripta **T166**, 014044 (2015). https://doi.org/10.1088/0031-8949/2015/t166/014044
41. X. Xu, W. Meng, P. Shuai et al., A data analysis method for isochronous mass spectrometry using two time-of-flight detectors at CSRe. Chin. Phys. C **39**, 106201 (2015). https://doi.org/10.1088/1674-1137/39/10/106201
42. P. Shuai, X. Xu, Y.H. Zhang et al., An improvement of isochronous mass spectrometry: velocity measurements using two time-of-flight detectors. Nucl. Inst. Methods Phys. Res. Sect. B Beam Interact. Mater. Atoms **376**, 311–315 (2016). https://doi.org/10.1016/j.nimb.2016.02.006
43. J. Xia, W. Zhan, B. Wei et al., The heavy ion cooler-storage-ring project (HIRFL-CSR) at Lanzhou. Nucl. Inst. Methods

Phys. Res. Sect. A Accel. Spectrom. Detect. Assoc. Equip. **488**, 11–25 (2002). https://doi.org/10.1016/S0168-9002(02)00475-8
44. W.W. Ge, Y.J. Yuan, J.C. Yang et al., Experimental investigation of the transition energy γ_t in the isochronous mode of the HIRFL-CSRe. Nucl. Inst. Methods Phys. Res. Sect. A Accel. Spectrom. Detect. Assoc. Equip. **908**, 388–393 (2018). https://doi.org/10.1016/j.nima.2018.08.059
45. Y.M. Xing, M. Wang, Y.H. Zhang et al., First isochronous mass measurements with two time-of-flight detectors at CSRe. Physica Scripta **T166**, 014010 (2015). https://doi.org/10.1088/0031-8949/2015/t166/014010
46. X.L. Yan, R.J. Chen, M. Wang et al., Characterization of a double Time-of-Flight detector system for accurate velocity measurement in a storage ring using laser beams. Nucl. Inst. Methods Phys. Res. Sect. A Accel. Spectrom. Detect. Assoc. Equip. **931**, 52–59 (2019). https://doi.org/10.1016/j.nima.2019.03.058
47. R.J. Chen, X.L. Yan, W.W. Ge et al., A method to measure the transition energy γ_t of the isochronously tuned storage ring. Nucl. Inst. Methods Phys. Res. Sect. A Accel. Spectrom. Detect. Assoc. Equip. **898**, 111–116 (2018). https://doi.org/10.1016/j.nima.2018.04.056
48. M. Zhang, Y. Zhang, M. Wang et al., Precision measurement of the transition energy t versus magnetic rigidity for storage-ring isochronous mass spectrometry. Nucl. Inst. Methods Phys. Res. Sect. A Accel. Spectrom. Detect. Assoc. Equip. **1027**, 166329 (2022). https://doi.org/10.1016/j.nima.2022.166329
49. M. Zhang, Y. Zhang, M. Wang, et al., Experimental study on the systematic deviation in the conventional isochronous mass spectrometry. Nucl. Phys. Rev. **40**, 181–187 (2023). https://doi.org/10.11804/NuclPhysRev.40.2022078
50. Y. Li, X. Wang, H. Zhang et al., Implementation of a dipole magnet power supply control system to improve magnetic field stability at the csre storage ring facility for precision mass measurement. Nucl. Inst. Methods Phys. Res. Sect. A Accel. Spectrom. Detect. Assoc. Equip. **1049**, 168108 (2023). https://doi.org/10.1016/j.nima.2023.168108
51. Y. Xing, Y. Zhang, M. Wang et al., Particle identification and revolution time corrections for the isochronous mass spectrometry in storage rings. Nucl. Inst. Methods Phys. Res. Sect. A Accel. Spectrom. Detect. Assoc. Equip. **941**, 162331 (2019). https://doi.org/10.1016/j.nima.2019.06.072
52. X.L. Tu, M. Wang, Y.A. Litvinov et al., Precision isochronous mass measurements at the storage ring CSRe in Lanzhou. Nucl. Inst. Methods Phys. Res. Sect. A Accel. Spectrom. Detect. Assoc. Equip. **654**, 213–218 (2011). https://doi.org/10.1016/j.nima.2011.07.018
53. M. Wang, Y.H. Zhang, X. Zhou et al., Mass measurement of upper *fp*-Shell $N = Z - 2$ and $N = Z - 1$ nuclei and the importance of three-nucleon force along the $N = Z$ line. Phys. Rev. Lett. **130**, 192501 (2023). https://doi.org/10.1103/PhysRevLett.130.192501
54. X. Zhou, M. Wang, Y.H. Zhang et al., Charge resolution in the isochronous mass spectrometry and the mass of ^{51}Co. Nucl. Sci. Tech. **32**, 37 (2021). https://doi.org/10.1007/s41365-021-00876-0
55. P. Shuai, H.S. Xu, X.L. Tu et al., Charge and frequency resolved isochronous mass spectrometry and the mass of ^{51}Co. Phys. Lett. B **735**, 327–331 (2014). https://doi.org/10.1016/j.physletb.2014.06.046
56. Y.H. Zhang, P. Zhang, X.H. Zhou et al., Isochronous mass measurements of $T_z = -1$ *fp*-shell nuclei from projectile fragmentation of ^{58}Ni. Phys. Rev. C **98**, 014319 (2018). https://doi.org/10.1103/PhysRevC.98.014319
57. X. Zhou, M. Wang, Y.H. Zhang et al., Mass measurements show slowdown of rapid proton capture process at waiting-point nucleus ^{64}Ge. Nat. Phys. **19**, 1091–1097 (2023). https://doi.org/10.1038/s41567-023-02034-2
58. M. Sun, Y. Yu, X. Wang et al., Ground-state mass of ^{22}Al and test of state-of-the-art *ab initio* calculations. Chin. Phys. C **48**, 034002 (2024). https://doi.org/10.1088/1674-1137/ad1a0a
59. P. Joss, X-ray bursts and neutron-star thermonuclear flashes. Nature **270**, 310–314 (1977). https://doi.org/10.1038/270310a0
60. R.K. Wallace, S.E. Woosley, Explosive hydrogen burning. Astrophys. J. Suppl. Ser. **45**, 389–420 (1981). https://doi.org/10.1086/190717
61. A. Bauswein, O. Just, H.T. Janka et al., Neutron-star radius constraints from GW 170817 and future detections. Astrophys. J. Lett. **850**, L34 (2017). https://doi.org/10.3847/2041-8213/aa9994
62. F.J. Fattoyev, J. Piekarewicz, C.J. Horowitz, Neutron skins and neutron stars in the multimessenger era. Phys. Rev. Lett. **120**, 172702 (2018). https://doi.org/10.1103/PhysRevLett.120.172702
63. A.W. Steiner, C.O. Heinke, S. Bogdanov et al., Constraining the mass and radius of neutron stars in globular clusters. Mon. Not. R. Astron. Soc. **476**, 421 (2018). https://doi.org/10.1093/mnras/sty215
64. T.E. Riley, A.L. Watts, P.S. Ray, et al., A NICER view of the massive pulsar PSR J0740+6620 informed by radio timing and XMM-newton spectroscopy. Astrophys. J. Lett. **918**, L27 (2021). arXiv:2105.06980, https://doi.org/10.3847/2041-8213/ac0a81
65. S. Koranda, N. Stergioulas, J.L. Friedman, Upper limits set by causality on the rotation and mass of uniformly rotating relativistic stars. Astrophys. J. **488**, 799 (1997). https://doi.org/10.1086/304714
66. H. Schatz, S. Gupta, P. Møller et al., Strong neutrino cooling by cycles of electron capture and $\beta-$ decay in neutron star crusts. Nature **505**, 62–65 (2014). https://doi.org/10.1038/nature12757
67. R. Lau, M. Beard, S.S. Gupta et al., Nuclear reactions in the crusts of accreting neutron stars. Astrophys. J. **859**, 62 (2018). https://doi.org/10.3847/1538-4357/aabfe0
68. M.Y. Fujimoto, Angular distribution of radiation from low-mass *X*-Ray binaries. Astroph. J. **324**, 995 (1988). https://doi.org/10.1086/165955
69. C.C. He, L. Keek, Anisotropy of X-ray bursts from neutron stars with concave accretion disks. Astroph. J. **819**, 47 (2016). https://doi.org/10.3847/0004-637X/819/1/47
70. Y.H. Lam, N. Lu, A. Heger et al., The regulated NiCu cycles with the new ^{57}Cu(p,γ)^{58}Zn reaction rate and its influence on type I X-ray bursts: the GS 1826–24 clocked burster. Astrophys. J. **929**, 73 (2022). https://doi.org/10.3847/1538-4357/ac4d89
71. Z. Meisel, G. Merz, S. Medvid, Influence of nuclear reaction rate uncertainties on neutron star properties extracted from X-ray burst model-observation comparisons. Astrophys. J. **872**, 84 (2019). https://doi.org/10.3847/1538-4357/aafede
72. W.J. Xie, B.A. Li, N.B. Zhang, Impact of the newly revised gravitational redshift of x-ray burster gs 1826-24 on the equation of state of supradense neutron-rich matter. (2024). arXiv:2404.01989
73. B.J. Cai, B.A. Li, Z. Zhang, Central speed of sound, the trace anomaly, and observables of neutron stars from a perturbative analysis of scaled Tolman-Oppenheimer-Volkoff equations. Phys. Rev. D **108**, 103041 (2023). https://doi.org/10.1103/PhysRevD.108.103041
74. M. Zhang, X. Xu, Y.M. Xing et al., Thermonuclear reaction rate of ^{57}Cu$(p,\gamma)^{58}$Zn in the *rp* process. Phys. Rev. C **109**, 045802 (2024). https://doi.org/10.1103/PhysRevC.109.045802
75. C. Langer, F. Montes, A. Aprahamian et al., Determining the *rp*-process flow through ^{56}Ni: Resonances in ^{57}Cu$(p,\gamma)^{58}$Zn identified with GRETINA. Phys. Rev. Lett. **113**, 032502 (2014). https://doi.org/10.1103/PhysRevLett.113.032502

76. H. Schatz, A. Aprahamian, V. Barnard et al., End point of the *rp* process on accreting neutron stars. Phys. Rev. Lett. **86**, 3471–3474 (2001). https://doi.org/10.1103/PhysRevLett.86.3471
77. J.Y. Zhang, R. Casten, D. Brenner, Empirical proton-neutron interaction energies. Linearity and saturation phenomena. Phys. Lett. B **227**, 1–5 (1989). https://doi.org/10.1016/0370-2693(89)91273-2
78. D. Brenner, C. Wesselborg, R. Casten et al., Empirical p-n interactions: global trends, configuration sensitivity and $N = Z$ enhancements. Phys. Lett. B **243**, 1–6 (1990). https://doi.org/10.1016/0370-2693(90)90945-3
79. P. Van Isacker, D.D. Warner, D.S. Brenner, Test of wigner's spin-isospin symmetry from double binding energy differences. Phys. Rev. Lett. **74**, 4607–4610 (1995). https://doi.org/10.1103/PhysRevLett.74.4607
80. I. Talmi, Effective interactions and coupling schemes in nuclei. Rev. Mod. Phys. **34**, 704–722 (1962). https://doi.org/10.1103/RevModPhys.34.704
81. P. Federman, S. Pittel, Towards a unified microscopic description of nuclear deformation. Phys. Lett. B **69**, 385–388 (1977). https://doi.org/10.1016/0370-2693(77)90825-5
82. R.F. Casten, Possible unified interpretation of heavy nuclei. Phys. Rev. Lett. **54**, 1991–1994 (1985). https://doi.org/10.1103/PhysRevLett.54.1991
83. R.B. Cakirli, R.F. Casten, Direct empirical correlation between proton-neutron interaction strengths and the growth of collectivity in nuclei. Phys. Rev. Lett. **96**, 132501 (2006). https://doi.org/10.1103/PhysRevLett.96.132501
84. K. Heyde, P. Van Isacker, R. Casten et al., A shell-model interpretation of intruder states and the onset of deformation in even-even nuclei. Phys. Lett. B **155**, 303–308 (1985). https://doi.org/10.1016/0370-2693(85)91575-8
85. P. Federman, S. Pittel, Hartree-Fock-Bogolyubov study of deformation in the Zr Mo region. Phys. Lett. B **77**, 29–32 (1978). https://doi.org/10.1016/0370-2693(78)90192-2
86. M. Hasegawa, K. Kaneko, Microscopic analysis of T=1 and T=0 proton-neutron correlations in $N = Z$ nuclei. Nucl. Phys. A **748**, 393–401 (2005). https://doi.org/10.1016/j.nuclphysa.2004.11.014
87. S. Goriely, N. Chamel, J.M. Pearson, Hartree-Fock-Bogoliubov nuclear mass model with 0.50 MeV accuracy based on standard forms of Skyrme and pairing functionals. Phys. Rev. C **88**, 061302 (2013). https://doi.org/10.1103/PhysRevC.88.061302
88. J. Duflo, A. Zuker, Microscopic mass formulas. Phys. Rev. C **52**, R23–R27 (1995). https://doi.org/10.1103/PhysRevC.52.R23
89. M. Kortelainen, J. McDonnell, W. Nazarewicz et al., Nuclear energy density optimization: large deformations. Phys. Rev. C **85**, 024304 (2012). https://doi.org/10.1103/PhysRevC.85.024304
90. N. Wang, M. Liu, X. Wu et al., Surface diffuseness correction in global mass formula. Phys. Lett. B **734**, 215–219 (2014). https://doi.org/10.1016/j.physletb.2014.05.049
91. T. Kawano, S. Chiba, H. Koura, Phenomenological nuclear level densities using the KTUY05 nuclear mass formula for applications off-stability. J. Nucl. Sci. Technol. **43**, 1–8 (2006). https://doi.org/10.1080/18811248.2006.9711062
92. P. Möller, A. Sierk, T. Ichikawa et al., Nuclear ground-state masses and deformations: FRDM(2012). At. Data Nucl. Data Tables **109–110**, 1–204 (2016). https://doi.org/10.1016/j.adt.2015.10.002
93. L. Geng, H. Toki, J. Meng, Masses, deformations and charge radii-nuclear ground-state properties in the relativistic mean field model. Prog. Theor. Phys. **113**, 785–800 (2005). https://doi.org/10.1143/PTP.113.785
94. P. Moller, J. Nix, W. Myers et al., Nuclear ground-state masses and deformations. At. Data Nucl. Data Tables **59**, 185–381 (1995). https://doi.org/10.1006/adnd.1995.1002
95. M. Karny, L. Batist, D. Jenkins et al., Excitation energy of the $T = 0\beta$-decaying 9^+ isomer in ^{70}Br. Phys. Rev. C **70**, 014310 (2004). https://doi.org/10.1103/PhysRevC.70.014310
96. D.G. Jenkins, N.S. Kelsall, C.J. Lister et al., $T = 0$ and $T = 1$ states in the odd-odd $N = Z$ nucleus, $^{70}_{35}$Br $_{35}$. Phys. Rev. C **65**, 064307 (2002). https://doi.org/10.1103/PhysRevC.65.064307
97. P. Schury, C. Bachelet, M. Block et al., Precision mass measurements of rare isotopes near $N = Z = 33$ produced by fast beam fragmentation. Phys. Rev. C **75**, 055801 (2007). https://doi.org/10.1103/PhysRevC.75.055801
98. I. Mardor, S.A.S. Andrés, T. Dickel et al., Mass measurements of As, Se, and Br nuclei, and their implication on the proton-neutron interaction strength toward the $N = Z$ line. Phys. Rev. C **103**, 034319 (2021). https://doi.org/10.1103/PhysRevC.103.034319
99. D.S. Brenner, R.B. Cakirli, R.F. Casten, Valence proton-neutron interactions throughout the mass surface. Phys. Rev. C **73**, 034315 (2006). https://doi.org/10.1103/PhysRevC.73.034315
100. P. Van Isacker, O. Juillet, F. Nowacki, Pseudo-SU(4) symmetry in pf-shell nuclei. Phys. Rev. Lett. **82**, 2060–2063 (1999). https://doi.org/10.1103/PhysRevLett.82.2060
101. K. Hebeler, S.K. Bogner, R.J. Furnstahl et al., Improved nuclear matter calculations from chiral low-momentum interactions. Phys. Rev. C **83**, 031301 (2011). https://doi.org/10.1103/PhysRevC.83.031301
102. Y.P. Wang, Y.K. Wang, F.F. Xu et al., Abnormal bifurcation of the double binding energy differences and proton-neutron pairing: nuclei close to $N = Z$ line from Ni to Rb. Phys. Rev. Lett. **132**, 232501 (2024). https://doi.org/10.1103/PhysRevLett.132.232501
103. J. Jänecke, Neutron-proton interaction in mirror nuclei. Phys. Rev. C **6**, 467–468 (1972). https://doi.org/10.1103/PhysRevC.6.467
104. Y.Y. Zong, C. Ma, Y.M. Zhao et al., Mass relations of mirror nuclei. Phys. Rev. C **102**, 024302 (2020). https://doi.org/10.1103/PhysRevC.102.024302
105. X.L. Yan, H.S. Xu, Y.A. Litvinov et al., Mass measurement of ^{45}Cr and its impact on the Ca-Sc cycle in X-ray bursts. Astrophys. J. **766**, L8 (2013). https://doi.org/10.1088/2041-8205/766/1/l8
106. A.P. Zuker, S.M. Lenzi, G. Martínez-Pinedo et al., Isobaric multiplet yrast energies and isospin nonconserving forces. Phys. Rev. Lett. **89**, 142502 (2002). https://doi.org/10.1103/PhysRevLett.89.142502
107. J. Ekman, D. Rudolph, C. Fahlander et al., Unusual isospin-breaking and isospin-mixing effects in the $A = 35$ mirror nuclei. Phys. Rev. Lett. **92**, 132502 (2004). https://doi.org/10.1103/PhysRevLett.92.132502
108. M.A. Bentley, C. Chandler, M.J. Taylor et al., Isospin symmetry of odd-odd mirror nuclei: Identification of excited states in $N = Z - 2^{48}$Mn. Phys. Rev. Lett. **97**, 132501 (2006). https://doi.org/10.1103/PhysRevLett.97.132501
109. A. Gadea, S.M. Lenzi, S. Lunardi et al., Observation of ^{54}Ni: cross-conjugate symmetry in $f_{7/2}$ mirror energy differences. Phys. Rev. Lett. **97**, 152501 (2006). https://doi.org/10.1103/PhysRevLett.97.152501
110. K. Kaneko, Y. Sun, T. Mizusaki et al., Variation in displacement energies due to isospin-nonconserving forces. Phys. Rev. Lett. **110**, 172505 (2013). https://doi.org/10.1103/PhysRevLett.110.172505
111. H.H. Li, Q. Yuan, J.G. Li et al., Investigation of isospin-symmetry breaking in mirror energy difference and nuclear mass with ab initio calculations. Phys. Rev. C **107**, 014302 (2023). https://doi.org/10.1103/PhysRevC.107.014302
112. J. Lee, X.X. Xu, K. Kaneko et al., Large isospin asymmetry in ^{22}Si/^{22}O mirror gamow-teller transitions reveals the halo

structure of ^{22}Al. Phys. Rev. Lett. **125**, 192503 (2020). https://doi.org/10.1103/PhysRevLett.125.192503
113. H.H. Li, J.G. Li, M.R. Xie et al., Ab initio calculations of mirror energy difference in sd-shell nuclei*. Chin. Phys. C **47**, 124101 (2023). https://doi.org/10.1088/1674-1137/acf035
114. J. Li, H. Li, S. Zhang et al., Double-magicity of proton drip-line nucleus ^{22}Si with ab initio calculation. Phys. Lett. B **846**, 138197 (2023). https://doi.org/10.1016/j.physletb.2023.138197
115. G.A. Miller, A.K. Opper, E.J. Stephenson, Charge symmetry breaking and QCD. Annu.Annu. Rev. Nucl. Part. Sci. **56**, 253–292 (2006). https://doi.org/10.1146/annurev.nucl.56.080805.140446
116. Z.C. Xu, S. Zhang, J.G. Li et al., Complex valence-space effective operators for observables: the gamow-teller transition. Phys. Rev. C **108**, L031301 (2023). https://doi.org/10.1103/PhysRevC.108.L031301
117. W. Benenson, E. Kashy, Isobaric quartets in nuclei. Rev. Mod. Phys. **51**, 527–540 (1979). https://doi.org/10.1103/RevModPhys.51.527
118. Y.H. Zhang, H.S. Xu, Y.A. Litvinov et al., Mass measurements of the neutron-deficient ^{41}Ti, ^{45}Cr, ^{49}Fe, and ^{53}Ni nuclides: first test of the isobaric multiplet mass equation in *fp*-shell nuclei. Phys. Rev. Lett. **109**, 102501 (2012). https://doi.org/10.1103/PhysRevLett.109.102501
119. M. MacCormick, G. Audi, Evaluated experimental isobaric analogue states from $T = 1/2$ to $T = 3$ and associated IMME coefficients. Nucl. Phys. A **925**, 61–95 (2014). https://doi.org/10.1016/j.nuclphysa.2014.01.007
120. Y.H. Lam, B. Blank, N.A. Smirnova et al., The isobaric multiplet mass equation for $A \leq 71$ revisited. At. Data Nucl. Data Tables **99**, 680–703 (2013). https://doi.org/10.1016/j.adt.2012.11.002
121. J.M. Dong, J.Z. Gu, Y.H. Zhang et al., Beyond Wigner's isobaric multiplet mass equation: effect of charge-symmetry-breaking interaction and coulomb polarization. Phys. Rev. C **99**, 014319 (2019). https://doi.org/10.1103/PhysRevC.99.014319
122. W.J. Huang, X. Zhou, Y.H. Zhang et al., Ground-state mass of the odd-odd $N = Z$ nuclide ^{70}Br. Phys. Rev. C **108**, 034301 (2023). https://doi.org/10.1103/PhysRevC.108.034301
123. J. Jänecke, Vector and tensor coulomb energies. Phys. Rev. **147**, 735–742 (1966). https://doi.org/10.1103/PhysRev.147.735
124. J.A. Nolen, J.P. Schiffer, Coulomb energies. Ann. Rev. Nucl. Sci. **19**, 471–526 (1969). https://doi.org/10.1146/annurev.ns.19.120169.002351
125. S. Shlomo, Nuclear coulomb energies. Rep. Prog. Phys. **41**, 957–1026 (1978). https://doi.org/10.1088/0034-4885/41/7/001
126. W.E. Ormand, Mapping the proton drip line up to $A = 70$. Phys. Rev. C **55**, 2407–2417 (1997). https://doi.org/10.1103/PhysRevC.55.2407
127. B.A. Brown, R.R.C. Clement, H. Schatz et al., Proton drip-line calculations and the rp process. Phys. Rev. C **65**, 045802 (2002). https://doi.org/10.1103/PhysRevC.65.045802
128. X. Zhou, J. Yang, the HIAF project team, Status of the high-intensity heavy-ion accelerator facility in China. AAPPS Bull. **32**, 35 (2022). https://doi.org/10.1007/s43673-022-00064-1
129. B. Wu, J. Yang, J. Xia et al., The design of the spectrometer ring at the HIAF. Nucl. Inst. Methods Phys. Res. Sec. A Accel. Spectrom. Detect. Assoc. Equip. **881**, 27–35 (2018). https://doi.org/10.1016/j.nima.2017.08.017
130. J. Yang, J. Xia, G. Xiao, et al., High intensity heavy ion accelerator facility (HIAF) in China. Nuclear Instruments and Methods in Physics Research Section B: Beam Interactions with Materials and Atoms **317**, 263–265 (2013). XVIth International Conference on ElectroMagnetic Isotope Separators and Techniques Related to their Applications, December 2-7, 2012 at Matsue, Japan. https://doi.org/10.1016/j.nimb.2013.08.046
131. J. Liu, J.C. Yang, J.W. Xia et al., Transverse impedances and collective instabilities in a heavy ion accelerator. Phys. Rev. Accel. Beams **21**, 064403 (2018). https://doi.org/10.1103/PhysRevAccelBeams.21.064403